Retrospective Theses and Dissertations

Iowa State University Capstones, Theses and Dissertations

1-1-1998

Growth and characterization of micro-crystalline silicon-germanium and silicon-carbon films

Karl Robert Erickson
Iowa State University

Follow this and additional works at: https://lib.dr.iastate.edu/rtd

Part of the Electrical and Computer Engineering Commons

Growth and characterization of micro-crystalline

Silicon-Germanium and Silicon-Carbon films

by

Karl Robert Erickson

A thesis submitted to the graduate faculty

in partial fulfillment of the requirements for the degree of

MASTER OF SCIENCE

Major: Electrical Engineering

Major Professor: Vikram L. Dalal

Iowa State University

Ames, Iowa

1998

Graduate College
Iowa State University

This is to certify that the Master's thesis of

Karl Robert Erickson

has met the thesis requirements of Iowa State University

Signatures have been redacted for privacy

To my wife, Deb

TABLE OF CONTENTS

LIST OF TABLES

LIST OF FIGURES

ABSTRACT

This thesis reports on the growth chemistry and appropriate process parameters that result in the formation of micro-crystalline silicon-germanium and silicon-carbon films. The growth technique uses an electron-cyclotron-resonance-chemical-vapor-deposition apparatus. This apparatus allows the process engineer to control such parameters as the plasma resonance plane, substrate temperature, microwave power, vacuum pressure, gas flow ratios, and gas combinations. The plasma gas is hydrogen and the precursor gases are silane and germane. The hydrogen ions and electrons in the plasma dissociate the precursor gases into radicals that give rise to film growth on the substrate. The substrate temperatures are kept below 300 °C so that deposition on polyimide substrates can be performed. High power (200 Watts) and low pressure (5 mTorr) typically results in micro-crystallite formation. However, it has been determined that micro-crystalline (Si,Ge):H only occurs for specific silane to germane ratios. The type of substrate (glass, polyimide, or molybdenum coated polyimide) also plays a role in the structure of the deposited films. Spectrophotometer, activation energy, conductivity, sub-gap absorption, and Raman spectroscopy measurements are used to characterize the film's optical, electrical, and structural properties. From these measurements, characteristic signatures have been established that determine the material's quality and structure. Relating the characterization data to the process parameters will allow the process engineer to precisely control the resulting semiconductor behavior in materials and devices during manufacturing.

CHAPTER 1. INTRODUCTION

Amorphous and micro-crystalline semiconductor materials are used in the manufacturing of solar cells, flat panel displays, thin film transistors, image sensors, and printer heads. These devices are but a few of the many semiconductor devices that are used by people throughout the world today. Understanding the growth processes of thin film semiconductors and their physical properties is critical for making smaller, faster, and higher quality devices. By no means is this understanding complete. New materials and alloys are constantly being explored with hopes of gaining more information and improving the performance of existing devices. With this rapidly changing environment, understanding the basic electrical, optical, and structural properties of amorphous, n-crystalline (where n-represents poly-, micro-, or nano-), and crystalline materials are necessary to determine the characteristics of new materials and their potential value to the semiconductor industry.

Structural Properties

Materials can be categorized into the following classes: crystalline, n-crystalline, and amorphous. Crystalline material has a uniform periodic lattice structure. Its physical properties are described through the use of the Bloch theorem [1]. On the other end of the spectrum, amorphous materials lack order. For amorphous materials, the Bloch theorem does not apply and description of the physical properties is carried out with the concept of localized and extended defect states [2 to 4]. The realm of n-crystalline materials lies between crystalline and amorphous materials. N-crystalline has a very broad meaning as the material is defined as having a periodic order of a range shorter than for crystalline materials.

Thus, the physical properties of n-crystalline materials are described by theories bounded by the Bloch theorem and the localized density of states concept [2 to 4]. The n- corresponds to the grain size or periodic order of the crystallites. Hence, grain sizes on the order of 10^{-9}, 10^{-6}, and 10^{-4} meters are called nano-, micro-, and poly-crystallites, respectively. Since these crystallites are embedded in an amorphous matrix, the properties of the film are determined by the amount and type of crystallite content. For poly-crystalline materials, the content of the amorphous volume is negligible and is located mainly at the grain boundaries; whereas for nano- and micro- crystalline materials, the amorphous volume is variable and decreases with increasing grain size [3].

For detailed discussion on the physical properties of these structural classifications, please refer to References [1 to 4].

Scope of Research

This thesis focuses on determining appropriate process parameters using the electron-cyclotron-resonance-chemical-vapor-deposition technique to make micro-crystalline materials. The alloys under study are combinations of group IV elements such as silicon, germanium, and carbon. To determine the structure and quality of the thin films, several optical and electrical characterization techniques are used. These characterization techniques include measuring the absorption coefficients with two different methods, photo and dark conductivities, activation energy, and Raman scattering. The resulting structure of the film is then correlated with the process parameters. This enables the process engineer to determine which of the many process parameters such as gas ratios and flow rates, substrate

temperature, deposition pressure, and microwave power has the greatest effect on the film's structure and quality.

CHAPTER 2. GROWTH TECHNIQUE

During the last decade, electron cyclotron resonance (ECR) plasma sources have been probed for their possible enhancement of current chemical vapor deposition (CVD) and ion beam semiconductor processing techniques. The growing consensus is that films grown with ECR plasma sources have better optical and electrical characteristics than films grown by the more conventional RF plasma sources [5,6]. A comparison of the physical advantages and disadvantages of ECR plasma sources to RF plasma sources are briefly summarized in the Table 2-1. As can be seen in Table 2-1, the advantages of ECR control of the plasma

Table 2-1. Comparison of ECR over RF operating at the same power.

ECR Plasma Source	RF Plasma Source
• Operation pressure is $\sim 10^{-4}$ - 10^{-3} Torr resulting in a controlled reaction volume.	• Operation pressure is $\sim 10^{-2}$ - 5 Torr resulting in uncontrolled reaction volume.
• Plasma generation zone is separate from the substrate area. Allows control of the energy of ions and electrons bombarding the substrate by varying a magnetic field.	• Plasma and substrate areas are not separated. No magnetic field to control the flow of ions and electrons.
• High ion density and controlled ion energies near the substrate $N_i > 10^{11}$ cm^{-3}.	• Lower ion density and uncontrolled ion energies near the substrate $N_i \sim 10^{10}$ cm^{-3}.
• Greater degree of gas decomposition resulting in higher concentrations of radicals and elemental species.	• Incomplete ionization and decomposition of process and plasma gases.
• Higher cost of equipment due to higher vacuum requirements and magnetic coils.	• Lower cost of equipment.
• More complex and larger system.	• Less complex and smaller system.
• Film deposition uniform over small areas.	• Film deposition uniform over large areas.

deposition conditions outweigh the plasma conditions of RF. Continued research on ECR systems to enlarge the area of deposition uniformity is in progress so that the disadvantage of area limitation can be removed. Once this problem is overcome, ECR systems will be the plasma enhancement system of choice for CVD production lines.

All samples presented in this study were deposited using an ECR plasma deposition system. The next sections will cover the basic principles behind ECR, the physical design of the ECR-CVD processing system used to grow micro-crystalline silicon, silicon-germanium, and silicon-carbon thin films, a brief discussion of the growth chemistry, the experimental procedure, and the metalization process used to deposit contacts for the electrical characterization of the films.

ECR Fundamentals

Electron cyclotron resonance is the condition where the microwave energy is coupled to the natural resonant frequency of the electron gas in a static magnetic field. This resonant frequency occurs when the electron cyclotron frequency, which is defined as

$$\omega_{ce} = \frac{q\,B}{m_e},\qquad\qquad(2\text{-}1)$$

equals the electron excitation frequency ω. When the static magnetic field strength is adjusted to resonance, $\omega_{ce} = \omega$, and a component of the electric field is perpendicular to the static magnetic field, the electrons are accelerated in a spiral fashion about the direction of the magnetic field lines due to the Lorentz force and in turn ionize and excite the neutral plasma gas. This process results in a low-pressure, almost collisionless, plasma that can be

varied from a weakly to a highly ionized state by changing the gas flow rates, input microwave power, and system vacuum pressure.

ECR systems are variable in size and shape, number, type, and position of magnets, and microwave introduction. The most common ECR arrangement is the Hitachi/NTT setup shown in Figure 2-1. The plasma source containment region is a stainless steel cavity that is bounded by two magnetic coils. The coils are used to generate the static magnetic field. Linearly polarized microwaves are introduced into the plasma source region through a quartz window via a rectangular waveguide. The three tuners allow the user to adjust the shape of the waveguide. The vacuum system pulls the plasma into the deposition chamber. The reader should note yet another advantage of the ECR system, namely the lack of a metal cathode that needs to be replaced over time in a RF system.
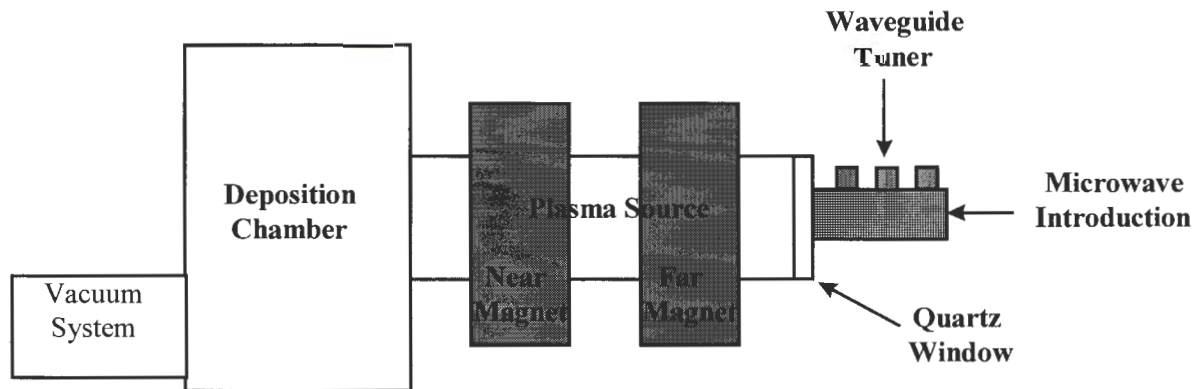
Figure 2-1. Typical Hitachi/NTT ECR arrangement.

Another feature of the ECR system is that the static magnetic field is capable of selecting a specific polarization of microwaves to be coupled into the plasma. Note that a linearly polarized wave can be written in the following general form:

$$E = Re\left[\frac{E_o}{2}\left(a_x + a_y\right)e^{i\omega t} + \frac{E_o}{2}\left(a_x - a_y\right)e^{i\omega t}\right] \qquad (2\text{-}2)$$

where the first component in the bracket is a right-hand circular polarized (RCP) wave and the second term is a left-hand circular polarized (LCP) wave. When the ECR condition is in effect, the electrons and the electric field vector of the RCP waves are rotating in phase with each other, while the LCP waves are rotating in the opposite direction. The net result is the energy from the RCP waves accelerates the electrons in the plasma and the plasma attenuates the energy from the LCP waves. LCP waves are completely attenuated when the critical density of plasma exceeds 7.5 x 10^{10} cm^{-3} for a 2.45 GHz source. The equation, derived from Maxwell's equations, used to calculate N$_{cr}$ is

$$N_{cr} = \frac{\omega \, \varepsilon_o \, m_e}{q^2} \, . \qquad (2\text{-}3)$$

Meanwhile, the accelerated electrons from RCP waves have gained the necessary energy to ionize the plasma gas and dissociate the process gases into free radicals.

More in-depth information about the fundamentals of ECR and the physics of plasmas can be found in References [6 to 11].

ECR-CVD System and Processing Conditions

The ECR-CVD system used in this research is shown in Figure 2-2. The system design closely follows the Hitachi/NTT system displayed in Figure 2-1. The reactor consists of the following components:

- A microwave source operating at 2.45 GHz.

- A rectangular waveguide system to transport the microwaves from the source to the plasma generation region. The system also contains three tuners with which
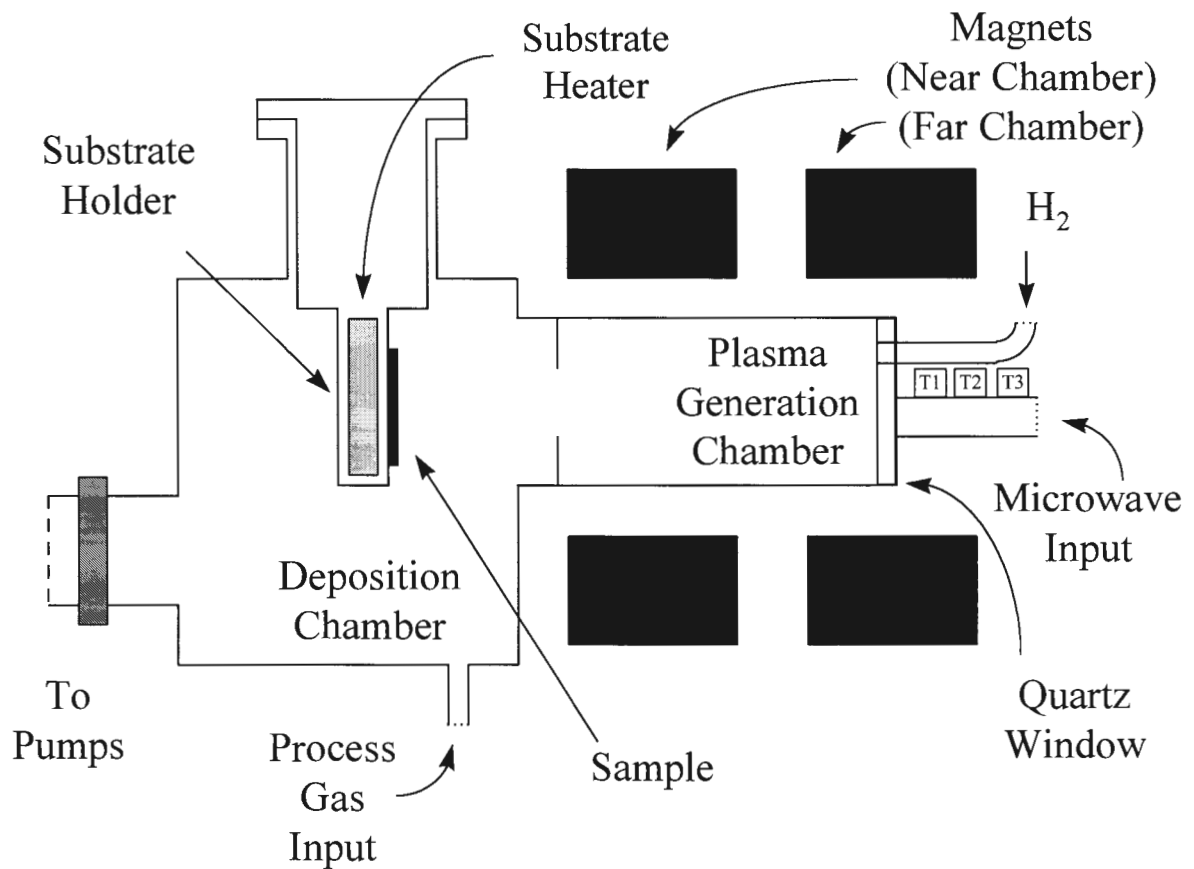
Figure 2-2. ECR-CVD apparatus.

to fine tune the polarization of the microwave. The tuner settings for all experiments in this study are T1 = 805, T2 = 810, and T3 = 705.

- The microwave power is coupled into the vacuum system near the plasma generation region through a quartz window.

- The ECR condition is established with the use of two magnetic coils. By adjusting the magnetic field strength of each coil, the position and strength of the ECR region within the plasma generation region can be controlled. Two DC power supplies rated at 10 V and 200 A are used to power the coils. For this system, it has been determined that the magnetic field profile is a maximum between 20 to 30 cm from the sample [12]. This maximum is the ECR resonance plane and corresponds to a current setting in the near magnet of $I_{near} \sim 178$ A, and $I_{far} \sim 183$ A in the far magnet. Depending on the conditions in the ECR-CVD reactor, the currents may vary slightly in order to obtain a minimum reflected power from the substrate. This corresponds to a maximum power transfer of the excited ions, atoms, and radicals from the plasma to the substrate.

- The restricting orifice provides uniformity of the plasma entering the deposition chamber and shapes the plasma into a diverging cone.

- The substrate holder uses a stainless steel mask to hold the substrate in place. Typical substrate sizes are 1 to 2 in^2 squares. In this experiment, the substrates are 7059 Corning glass, low-temperature polyimide, and polyimide coated with molybdenum. The substrate holder also contains a heater block in the region of

the substrate. For this study, the majority of the depositions are carried out with substrate temperatures below 280 °C.

- The vacuum system contains a roughing pump to bring the pressure from atmospheric pressure to 10^{-3} Torr and a turbo molecular pump to bring the base pressure down to the 10^{-7}-10^{-8} Torr region for deposition. The turbo molecular pump is backed by a roots blower pump and a mechanical pump. All pumps are constantly purged with nitrogen to prevent build up of any residual toxic gases.

- Plasma gases such as hydrogen and helium are introduced in the far end of the plasma source chamber through a separate manifold. These gases are ionized and with the help of electrons they can dissociate the process gases into radicals. The process gases (silane, germane, and trimethylboron) are injected into the deposition chamber near the substrate. Trimethylboron is used for enhancing the material's electrical properties and reducing the number of defect states. Depositions are performed with chamber pressures between 5 and 10 mTorr.

Growth Chemistry

Electrical and optical properties of a material are determined by the growth chemistry during the deposition. Growth chemistry from plasma sources is highly complex and not fully understood due to the formation of many sub-species of radicals that are deposited on the substrate. Factors that affect the growth chemistry are chamber pressure, microwave power, substrate temperature, gas flow rates, and gas combinations.

As the pressure in the ECR-CVD reactor is reduced, the energy and the flux of H ions

increases causing the plasma density to maximize between 5 and 10 mTorr (see Figure 2-3) [13]. Therefore, at low pressures, the growing film is subjected to increased ion bombardment and to increased etching due to the higher density of H radicals. The larger energy H ions are able to break weaker bonds and the net result is a more homogenous film growth. A similar effect can be achieved by increasing the microwave power. This etching-during-growth technique preferentially removes the weak, amorphous bonds leaving behind crystalline bonds. Thus, to promote micro-crystalline film growth one should use low-pressure and high-power. Typical settings for the ECR-CVD system for depositing micro-crystalline films are a pressure of 5 mTorr and a power of 212 Watts. One drawback to these conditions is that the growth rate is reduced due to the increased etching.

Substrate heating provides thermal energy to reduce the number of weak bonds being incorporated into the film. This is an important feature when depositions can be carried out at temperatures > 500 °C. The result of high-temperature film growth is a crystalline film. However, by using the high-power, low-pressure technique, micro-crystalline films can be grown at temperatures as low as 250 °C. These low temperatures are required if depositions on flexible polyimide substrates are to be possible.

Film growth is achieved by the radicals initially attaching themselves to the substrate and then growing epitaxially. Clearly, the lattice structure and material of the substrate play a role in the structure of the deposited film [14]. However, micro-crystalline films can be formed on amorphous glass substrates with the proper precursor gas concentrations and hydrogen dilution. Figure 2-4 steps through the epitaxial process for silane radicals.
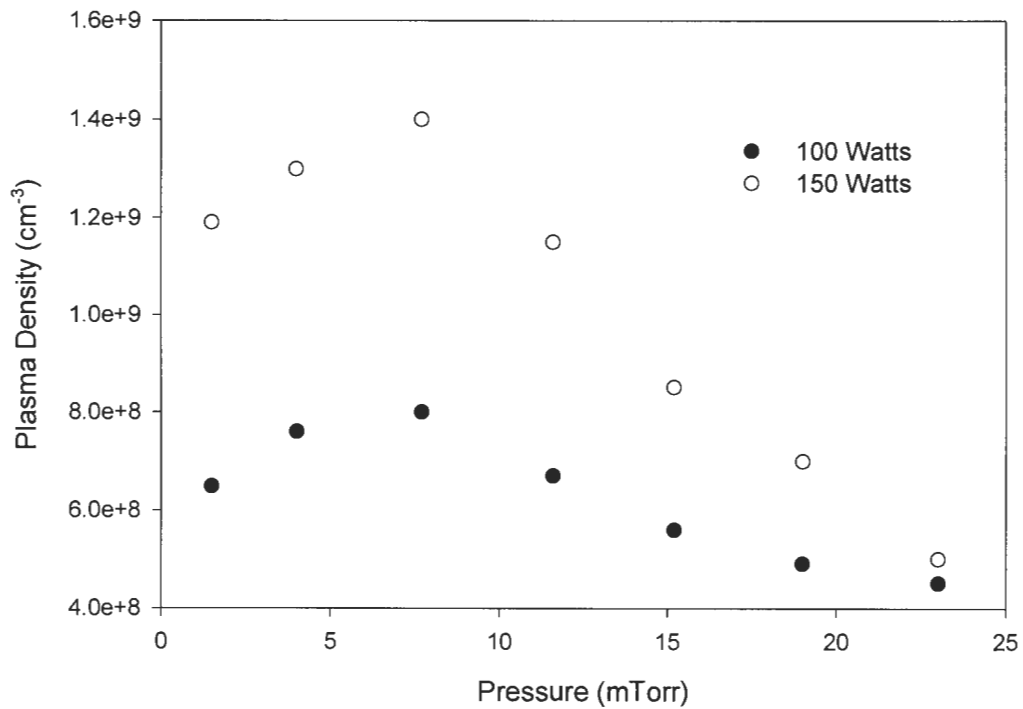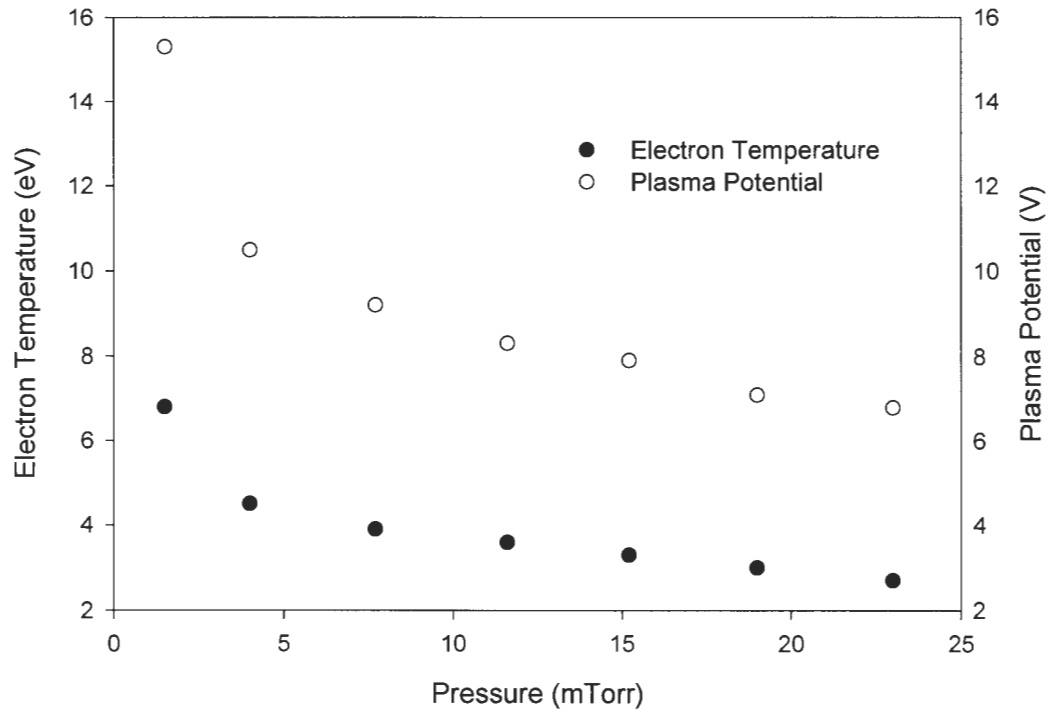
Figure 2-3. Langmuir probe measurements taken by Scott Deboer that show various plasma parameters with pressure [13].

Remember that in a plasma, several chemical reactions can take place when dissociation of the precursor gases occurs. As an example, silane (SiH$_4$) can be broken down into SiH$_3$, SiH$_2$, and SiH radicals. Similar radicals are produced in the dissociation of germane (GeH$_4$); however, the rate of dissociation is different due to the difference in bond strengths. Each of the radical's forms different bonds in the epitaxial growth that together lead to hills, valleys, and voids (see growth types 1 to 3 in Figure 2-4).

Type 1: All radicals present

Type 2: Non homogenous growth

Type 3: Formation of a void

Type 4: Homogenous growth

H$_2$ Bond Will Form

Passive Site

Active Site
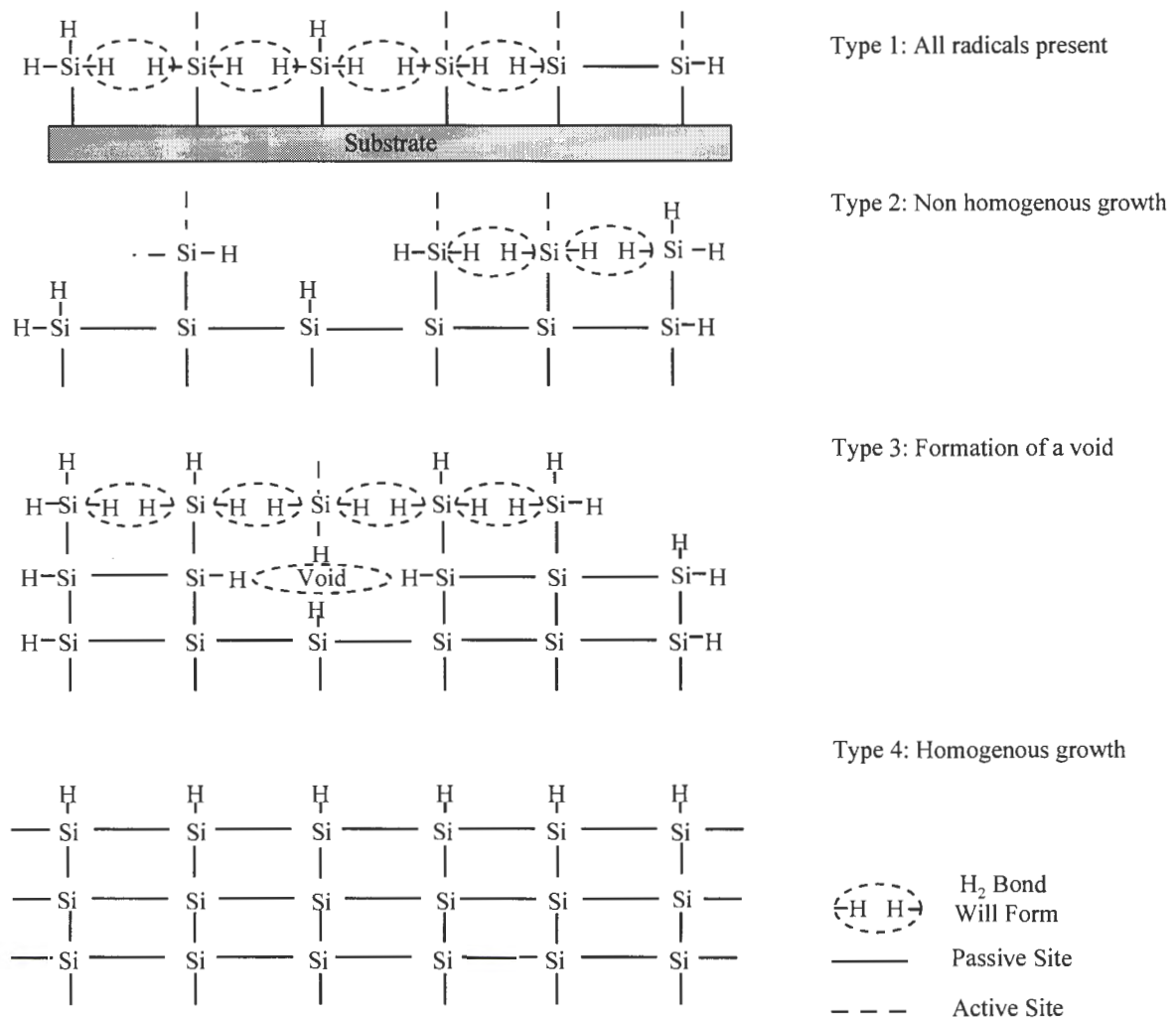
Figure 2-4. Possible epitaxial growth conditions.

Thus, this multi-species growth leads to a non-homogenous film that results in a material of poor quality. It should be noted that depositions with a high substrate temperature self-correct these defects. Therefore, low-temperature depositions require that the process engineer take measures to ensure that only one of the radical structures is incorporated into the film growth.

Selection of the SiH_3 or GeH_3 radical can be achieved with hydrogen dilution. The predictable chemical reactions are

$$SiH_4 + H \longrightarrow H_2 + SiH_3 \qquad (2\text{-}4)$$

$$GeH_4 + H \longrightarrow H_2 + GeH_3 \qquad (2\text{-}5)$$
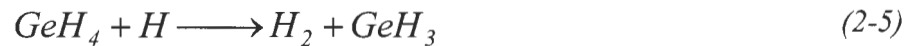
Thus, the excess H forces the production of the SiH_3 and GeH_3 radicals. Also, the excess H atoms will see the three Si - H bonds or Ge - H bonds and break them to form H_2 gas, allowing Si - Si, Si - Ge, or Ge - Ge bonds to form. Therefore, surface homogenization is achieved by the deposition of SiH_3 and GeH_3 radicals and H passivating any active sites. This *a priori* chemistry results in the homogenous growth (see Type 4) depicted in Figure 2-4.

Growth Procedure

In an effort to maintain repeatability of film growth, a strict standard operating procedure is followed. The first step involves cleaning the substrate. The standard cleaning procedure consists of boiling the substrate for 10 minutes in acetone followed by 10 minutes in methanol. The substrate is blown dry using nitrogen just before being mounted on the

substrate holder. The substrate holder is immediately loaded into the ECR-CVD system and a series of nitrogen, hydrogen, and silane purges are performed to help remove any remaining moisture in the system. In between purges, the substrate temperature is raised to 50 °C above the desired deposition temperature. Following the purges, a shutter is placed in front of the substrate to prevent film deposition during the chamber etch and dummy layer growth. A hydrogen plasma is lit to perform an etch of the chamber walls. This removes any impurities that might have been deposited during a previous experiment. 100% silane is introduced into the plasma for a dummy layer. This places a fresh layer of silicon on the chamber walls and covers up any remaining impurities left on the chamber walls. During this procedure, the substrate heater is adjusted to the desired temperature. Prior to opening the shutter, the 100% silane is replaced with hydrogen diluted 10% silane and the 10% germane in the desired proportions and the hydrogen flow is adjusted to achieve the desired H to Si to Ge ratios. Film deposition times ranged from two to six hours depending on the growth rate and desired film thickness. Upon completion of the deposition, the plasma is turned off and the film is left to cool down to below 100 °C before being pulled out. While cooling, the chamber is back filled with 1 Torr of H_2 and SiH_4 to prevent oxidation. The film is now ready to be characterized. Optical measurements covering the absorption, reflection, and transmission characteristics are performed before electrical measurements. This is because metal contacts need to be evaporated onto the films. The following section covers the metalization procedure.

Metalization

To measure the electrical properties of the films, chromium contacts are evaporated onto the films by a thermal evaporator. The evaporator system consists of a diffusion pumped bell jar with resistively heated chromium rods. A mask, as shown in Figure 2-5, is placed in front of the film. The openings in the mask provide a L/W ratio of 20. After the film/mask combination is loaded into the evaporator chamber, the bell jar is pumped to a base pressure in the range of $3*10^{-6}$ Torr before the evaporation is started. The chromium layer is deposited at an average rate of 5 A/sec and the thickness is approximately 1000 A as measured by a thickness monitor inside the evaporator. Silver paint is applied on top of the chromium contacts to provide a good contact to the metal probes. The conductive paint also helps to reduce contact resistance. The samples are then annealed at 160 °C for at least 30 minutes.
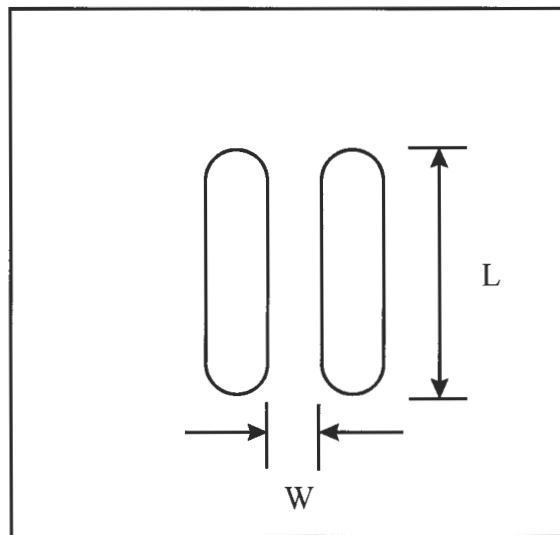
Figure 2-5. Metal mask used to evaporate contacts on the films.

CHAPTER 3. CHARACTERIZATION TECHNIQUES

To analyze the optical and electrical properties of the thin films prepared by the ECR-CVD system many measurements are performed. These measurements include UV/VIS/NIR spectroscopy, photo and dark conductivity, sub-band gap absorption, activation energy, and Raman spectroscopy. Using this data, it is possible to determine the presence and quality of micro-crystalline structures in the films. Since not all research labs are equipped with a Raman spectrometer, it is also possible to establish numerical and trend guidelines, based on the other four measurement techniques that predict the presence of micro-crystalline structures. Thus, these techniques will enable the process engineer to incorporate specific film qualities into devices, such as solar cells and thin film transistors.

UV/VIS/NIR Spectroscopy

The Perkin Elmer Lambda-9 dual beam spectrophotometer provides multiple functions in film characterization. The sophisticated apparatus is self-calibrating, consists of a sample and a reference beam, and acquires data via computer control. Depending on the range of wavelength operation, the user can use transmission and reflection data to quickly obtain the film thickness and the user can use absorption and reflection data to determine the absorption coefficients of the film. From this data the E_{04} energy gap and E_T Tauc gap can be determined for each film.

In the wavelength range of 1000 nm to 2500 nm, the interference peaks in the reflection and transmission scans are a result of scattering, since it is assumed that the film is non-absorbing over this range. The relationship to calculate the thickness is

$$t = \frac{\lambda_1 \lambda_2}{\beta n |\lambda_1 - \lambda_2|} \qquad (3\text{-}1)$$

where $\beta = 2$ for peak to peak intervals and $\beta = 4$ for the peak to valley intervals. The refractive index of the film is determined by solving for n in the expression

$$Avg\langle R \rangle = \left(\frac{n-1}{n+1} \right)^2 \qquad (3\text{-}2)$$

where Avg<R> is the average reflection coefficient in the non-absorbing range. It is known that the index of refraction varies with wavelength; however, within this non-absorbing range the variance of refractive indices is small. As a result, the refractive index is assumed to be constant over the range of wavelength used. This assumption leads to a thickness accuracy of ∓ 0.1 μm.

For wavelengths less than $\lambda_{bandgap}$, the films experience absorption. Using the expressions

$$A(\lambda) = Log_{10} \frac{1}{T(\lambda)} \qquad (3\text{-}3)$$

$$T(\lambda) = [1 - R(\lambda)] e^{-\alpha(\lambda)t} \qquad (3\text{-}4)$$

where $A(\lambda)$ is absorption, $T(\lambda)$ is transmission, $R(\lambda)$ is reflection, t is thickness, and $\alpha(\lambda)$ is the absorption coefficient, the absorption coefficient can be calculated. Solving Equation (3-3) for $T(\lambda)$ and substituting the result into Equation (3-4) yields the following expression for the absorption coefficient in terms of absorption and reflection data.

$$\alpha(\lambda) = \frac{Ln[1 - R(\lambda)] + 2.303 \, A(\lambda)}{t} \qquad (3\text{-}5)$$

A plot of $\alpha(\lambda)$ vs. E_{ph} provides visual information about the absorption edge. The knee of the curve typically occurs around $\alpha(\lambda) = 10^4$ cm^{-1} which is denoted as the E_{04} energy gap. A plot of $(\alpha(\lambda)*E_{ph})^{1/2}$ vs. E_{ph} yields a straight line that when extrapolated down to the E_{ph} axis determines the Tauc gap, E_T, of the film.

Photo and Dark Conductivity

Conductivity measurements provide early insight to the electronic film's quality and structure. To measure the dark, σ_d, and photo, σ_{ph}, conductivity, the sample is placed on a base and probes are connected to the sample contacts. A light source is mounted directly above the sample to illuminate the sample with a spectrum similar to the sun. The light source luminosity is calibrated to the strength of the sun. The whole apparatus is enclosed in a chamber that prevents any photo generation of charge carriers when the light source is off. There is a fan that keeps the sample at or near room temperature.

For measurements of dark and photo conductivity, a voltage of 100 V is applied across the sample and the current is measured using a highly sensitive ammeter. Thus, the conductivity is determined by the expression

$$\sigma_{d,ph} = \frac{W\,I}{L\,V\,t} \tag{3-6}$$

where W/L is the length to width ratio of the metal contacts, which is 20, t is the film thickness, and I is the measured current.

Dark conductivity arises from thermal generation and recombination processes of free carriers. When free carriers (electrons and holes) in a semiconductor reach their thermal equilibrium they contribute to conductivity of the material as

$$\sigma = q\, n_o\, \mu_n + q\, p_o\, \mu_p \qquad (3\text{-}7)$$

where μ_n and μ_p are the electron and hole mobilities, respectively. Since σ is known, the transport properties of the film can be explored. In terms of structural properties, amorphous materials will have dark conductivities in the 10^{-9} to 10^{-11} range while micro-crystalline materials will have dark conductivities in the 10^{-2} to 10^{-5} range.

Photo conductivity occurs when carriers are optically excited from the non-conducting to the conducting states. In this case, the conductivity is a function of the photo generation, thermal generation, and recombination of free carriers. As a result of the additional photo generation processes, the conductivities increase. The material's quality and structure determine the amount of increase.

The ratio of the photo to dark conductivity is known as the photo sensitivity. Since the light intensity is the same for all the samples, the photo sensitivity is an indication of how well the material can collect the photo generated carriers. Thus, this ratio can be used to determine how well the film would function as a detector. Clearly, a larger ratio would make sensing an on/off characteristic easier.

Sub-Band Gap Absorption

The two-beam photo conductivity sub-band gap absorption technique developed by Wronski and co-workers [15], accurately probes the absorption sub-gap states below

$\alpha = 10^2 \, \text{cm}^{-1}$. Since the majority of films prepared by the ECR-CVD technique are less than 10 μm thick, thin film geometry limits the accurate determination of α from absorption and reflection data taken by the spectrophotometer to α's greater than $10^2 \, \text{cm}^{-1}$. Another benefit of the two-beam sub-gap technique is that it enables the determination of absorption coefficients for films grown on non-transparent substrates such as stainless steel, polyimide, and molybdenum coated polyimide.

This two-beam photo conductivity technique utilizes a DC light beam of high intensity to fix the quasi Fermi levels (and hence carrier lifetimes), while an AC light beam of low intensity probes the photo conductivity of the sample (see Figure 3-1).
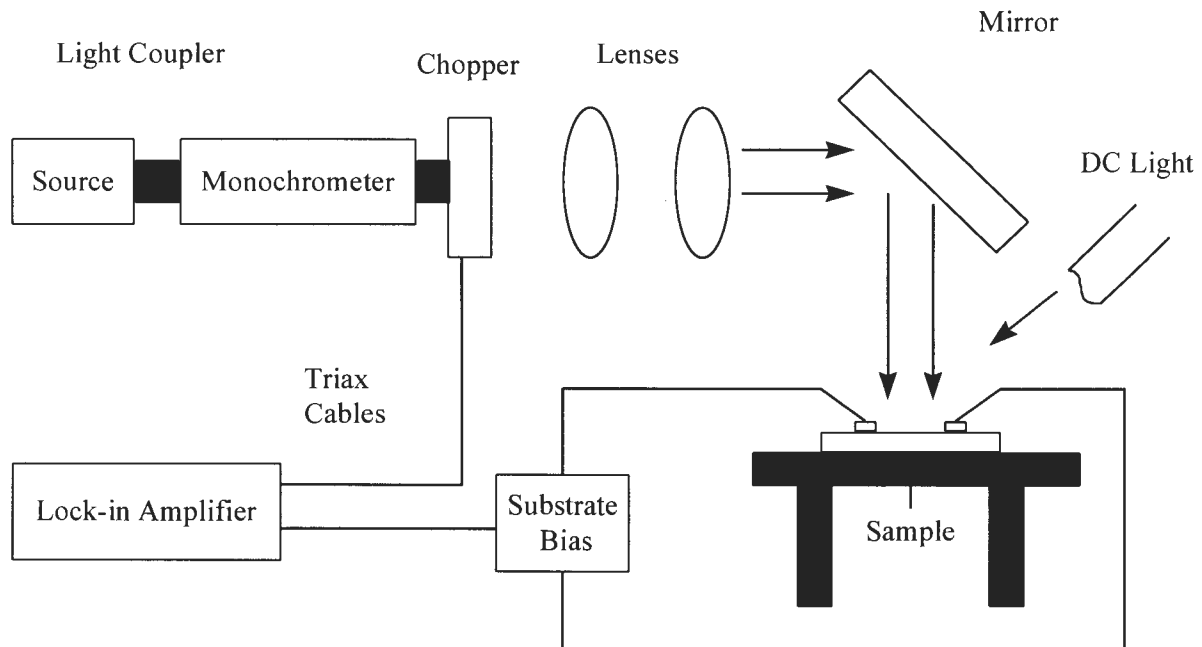

Figure 3-1. Apparatus for measuring sub-band gap absorption coefficients.

More specifically, the DC beam continuously creates electron-hole pairs that keep the traps filled and the occupancy of the mid-gap states constant. This fixes the lifetimes of the photo generated carriers. Meanwhile, the AC beam superimposes on the DC beam and thus modulates the creation of additional electron-hole pairs that can be detected by a lock-in amplifier. This photo generated signal can be used to determine the absorption coefficient. To enhance the measured signal, a bias of 5 volts is placed across the sample to improve the transport of electron-hole pairs. The absorption coefficient is calculated at each wavelength by dividing the signal by a reference signal and multiplying by the quantum efficiency of the Si reference detector.

In the experimental apparatus shown in Figure 3-1, the source is a white light and the monochrometer is used to change the wavelength of the incident photons. The range of the wavelengths used in the measurement is from 400 nm to 1100 nm for Si films. Chopping the output of the monochrometer at 13.5 Hz creates the AC beam. This frequency produces a square wave and reduces the noise due to ambient light and 60 Hz power lines. High pass optical filters are added at 700 nm and 800 nm to reduce second harmonics from the monochrometer and to prevent photons of lower wavelengths from reaching the sample. The AC beam is collimated using two lenses and focused down onto the sample between the probe contacts with a mirror. Since the lifetime of the electron-hole pairs is constant, due to the DC light, the photo current corresponds directly to the absorption coefficient. Also, since the signal is detected with a lock-in amplifier only the photo current corresponding to the chopper frequency is detected. If one wants to match the photo conductivity absorption

coefficients to the spectrophotometer absorption coefficients, a procedure is explained in Appendix B [12].

In this study, matching the curves is not important when determining the structure and quality of the material. What is important is the sub-gap data in the range between 1.0 to 2.0 eV. By plotting α vs. energy, the trend of the curve can be compared to the trend of a crystalline Si absorption curve [16]. A crystalline trend has a rounded curve, while an amorphous trend has a curve that sharply drops to zero. Since the exact composition of the (Si,Ge):H is not known, the curves are arbitrarily normalized to the crystalline Si curve at 1.5 eV. Thus, the shape of this curve is an electronic indication of the film's structure. The more closely the shape of the curve matches the crystalline Si curve the more likely the film is to consist of micro-crystalline structures. The film's quality can be qualitatively determined by the amount of noise present in the photo current at these low absorption coefficients.

Activation Energy

This characterization technique measures the activation energy due to the thermal excitation. Due to the difference in transport theories between amorphous, n-crystalline, and crystalline materials, the activation energy has different meanings. Transport theory for amorphous films says that the activation energy can be used to directly determine the Fermi energy; however for crystalline films, transport theory states that the activation energy is merely the energy required to get current flow between the grain boundaries. Thus, the slope of the Arrhenius plot reveals the material's structure. A positive slope corresponds to a

crystalline film. A slightly negative slope corresponds to a n-crystalline film. A large negative slope corresponds to an amorphous film.

In this technique, the substrate rests on a heater block inside an enclosed box. This eliminates any excitation due to photon absorption. To enhance the current, a bias of 100 V is applied between the probes. The temperature ranges from 180 °C to 80 °C and the activation energy is calculated by the Arrhenius relationship

$$I = I_o e^{-\frac{E_A}{k_B T}} \qquad (3\text{-}8)$$

where I is the phonon current, I_o is a prefactor current, k_B is Boltzman's constant, and T is the sample temperature in Kelvin. Substituting Equation (3-8) into Equation (3-6) provides activation energy information in terms of the film's conductivity. The temperature is not allowed to exceed 200 °C as this prevents any changes in the bond structure from occurring. By plotting the $Ln(I/I_o)$ vs. 1000/T, the slope of the linear line is the activation energy. The lower the activation energy the greater the possibility the film contains some degree of crystallinity. Clearly, this makes sense because it takes more energy to activate current flow in an amorphous film than in a crystalline film [17].

Raman Spectroscopy

Raman scattering phenomena provides direct insight into the degree of structure crystallinity within the film. The basis of the Raman effect is the inelastic scattering of an incident photon by the film through creation or annihilation of a phonon. Since Raman scattering is related to the inelastic scattering of incident photons by the molecular vibrations

and rotations of the film, the resonance frequencies are signatures of the film's material and structural composition. The sharpness of the peak can be related to the film's structure. The Raman resonance peak is directly related to the amount of relaxation of the momentum conservation in the scattering process. A broad low intensity peak is a sign of large relaxation in amorphous materials, while a sharp high intensity peak is a sign of little relaxation in crystalline materials.

Detection of this scattering phenomenon is in terms of (-) Stokes and (+) Anti-Stokes wavenumber shifts from equilibrium. Typically, the intensity of the Stokes shift is larger than the Anti-Stokes shift. Scattering from an induced dipole moment results in a polarized signal along either the longitudinal (LO) or the transverse (TO) optic axes [18]. Fortunately, crystalline Si and Ge, do not have a polarization difference between LO and TO modes. This simplifies the required detection optics of the scattering events. The first order TO/LO Raman peaks are 521 cm^{-1} for Si and 301 cm^{-1} for Ge [19]. GeSi films deposited by thermal and excimer laser CVD exhibit three peaks due to Ge-Ge, Ge-Si, and Si-Si modes near 300, 400, and 500 cm^{-1}, respectively [20]. Similar results will be presented in the next chapter with (Si,Ge):H films deposited using the ECR-CVD technique.

The films are measured using a Raman apparatus consisting of a Coherent Innova 200 Argon ion laser operating at 488 nm CW and 50 mW, a Spex Triplemate double monochrometer system, and a liquid nitrogen cooled CCD detector [21].

CHAPTER 4. RESULTS

To readily analyze the results of this work, the data has been divided into 2 groups based on the pressure at which the samples were grown. The deposition parameters are as follows: a substrate temperature of 280 ºC and a microwave power of 212 Watts. Tables 4-1 and 4-2 contain the deposition conditions for a small sampling of the experiments performed at 5 mTorr and 10 mTorr, respectively. Similarly, Tables 4-3 and 4-4 contain a summary of the optical and electrical properties. This data set also contains comparisons between films grown on 7059 Corning glass, polyimide, and molybdenum coated polyimide substrates.

The majority of the films were Si_xGe_{1-x} alloys where silane to germane ratios were high. However, a few experiments were performed with the roles of silane and germane reversed. Unfortunately, experiments of depositing Si_xC_{1-x} alloys using silane and methane were not fruitful, as good data on the electrical and optical properties was difficult to obtain. There is information concerning this alloy at the end of the chapter. In all three cases, the ratio of hydrogen to the dominant process gas was 40:1. Hydrogen dilution at this ratio is known to produce micro-crystalline Si films when silane is used as the only feed gas [22]. However, it will be shown that this ratio does not produce micro-crystalline Ge films when germane is used as the only feed gas.

This chapter will show that electronic and optical measurements can be used to predict the material's structure and quality. Verification of these predictions is achieved by performing Raman spectroscopy. Also, correlation of these results with the deposition parameters will show that gas flow ratios are just as important as the vacuum pressure, substrate temperature, and microwave power when growing micro-crystalline films.

Table 4-1. Deposition conditions of (Si,Ge):H films at 5 mTorr.

		Gas	Flow	Rates	Gas	Flow	Ratios
		100 %	10 %	10 %	H_2 to	H_2 to	SiH_4 to
	Time	H_2	SiH_4	GeH_4	SiH_4	GeH_4	GeH_4
Sample #	(min)	(%)	(%)	(%)	(sccm)	(sccm)	(sccm)
2-2048	120	24	50	-	40:1	-	-
**2-2241	120	24	50	-	40:1	-	-
2-2536	180	12	25	5	40:1	352:1	8.8:1
2-2561	180	12	25	10	40:1	176:1	4.4:1
2-2764	120	12	25	15	40:1	117:1	2.93:1
2-2506	120	12	25	20	40:1	88:1	2.2:1
*2-2311	240	12	25	20	40:1	88:1	2.2:1
2-2763	120	12	25	25	40:1	70.4:1	1.76:1
2-2505	120	12	25	30	40:1	59:1	1.475:1
2-2482	120	12	25	44	40:1	40:1	1:1
2-2504	120	12	25	50	40:1	35:1	0.875:1
2-2765	120	12	-	44	-	40:1	-
2-2766	120	12	5	44	200:1	40:1	0.2:1
2-2767	120	12	10	44	100:1	40:1	0.4:1
2-2768	120	12	15	44	66.6:1	40:1	0.6:1
2-2769	120	12	20	44	50:1	40:1	0.8:1

Note: ** in sample # column indicates polyimide substrate, while * indicates molybdenum coated polyimide substrate.

Table 4-2. Deposition conditions of (Si,Ge):H films at 10 mTorr.

		Gas	Flow	Rates	Gas	Flow	Ratios
		100 % H_2	10 % SiH_4	10 % GeH_4	H_2 to SiH_4	H_2 to GeH_4	SiH_4 to GeH_4
Sample #	Time (min)	(%)	(%)	(%)	(sccm)	(sccm)	(sccm)
*2-2280	180	24	50	10	40:1	352:1	8.8:1
2-2530	180	12	25	5	40:1	352:1	8.8:1
2-2531	180	12	25	10	40:1	176:1	4.4:1
2-2532	120	12	25	20	40:1	88:1	2.2:1
2-2533	120	12	25	30	40:1	59:1	1.475:1
2-2534	120	12	25	44	40:1	40:1	1:1
2-2535	120	12	25	50	40:1	35:1	0.875:1

Note: * in sample # column indicates molybdenum coated polyimide substrate.

Table 4-3. Electrical and optical properties of (Si,Ge):H films at 10 mTorr.

Sample #	Thickness (μm)	Growth Rate (A/sec)	E_{04} (eV)	E_T (eV)	σ_{ph} (S/cm)	σ_d (S/cm)	Photosens. (σ_{ph}/σ_d)	E_A (eV)
*2-2280	0.95	0.88	-	-	$0.34e^{-2}$	$0.31e^{-2}$	1.1	0.10
2-2530	0.49	0.45	2.00	1.81	$0.3e^{-5}$	$1.2e^{-8}$	$2.5e^{+2}$	0.46
2-2531	0.64	0.59	1.95	1.89	$0.3e^{-4}$	$0.7e^{-9}$	$4.29e^{+4}$	0.69
2-2532	0.57	0.79	1.84	1.65	$0.2e^{-4}$	$1.0e^{-9}$	$2.0e^{+4}$	0.59
2-2533	0.62	0.85	1.71	1.55	$0.8e^{-5}$	$1.4e^{-9}$	$5.71e^{+3}$	0.60
2-2534	0.87	1.21	1.60	1.43	$0.3e^{-5}$	$0.7e^{-8}$	$4.28e^{+2}$	0.55
2-2535	0.99	1.37	1.56	1.40	$0.3e^{-5}$	$0.8e^{-8}$	$3.75e^{+2}$	0.55

Note: * in sample # column indicates molybdenum coated polyimide substrate.

Table 4-4. Electrical and optical properties of (Si,Ge):H films at 5 mTorr.

Sample #	Thickness (μm)	Growth Rate (A/sec)	E_{04} (eV)	E_T (eV)	σ_{ph} (S/cm)	σ_d (S/cm)	Photosens. (σ_{ph}/σ_d)	E_A (eV)
2-2048	0.82	1.13	2.09	1.80	$0.2e^{-2}$	$0.2e^{-2}$	1.0	0.11
**2-2241	1.06	1.47	-	-	$1.82e^{-7}$	$0.3e^{-11}$	$6.07e^{+4}$	0.84
2-2536	0.74	0.69	2.05	1.88	$0.25e^{-3}$	$1.4e^{-4}$	1.79	0.18
2-2561	0.75	0.69	1.92	1.79	$0.35e^{-3}$	$0.2e^{-3}$	1.75	0.16
2-2764	0.53	0.74	1.86	1.75	$0.54e^{-4}$	$1.68e^{-5}$	3.21	0.27
2-2506	0.58	0.81	1.83	1.63	$0.21e^{-4}$	$0.46e^{-6}$	$4.56e^{+1}$	0.39
*2-2311	1.21	0.84	-	-	$0.28e^{-2}$	$0.27e^{-2}$	1.04	0.19
2-2763	0.75	1.04	1.73	1.55	$1.1e^{-5}$	$0.9e^{-7}$	$1.22e^{+2}$	0.45
2-2505	0.94	1.31	1.69	1.52	$0.25e^{-5}$	$1.7e^{-9}$	$1.47e^{+3}$	0.62
2-2482	0.91	1.26	1.60	1.42	$0.41e^{-5}$	$0.67e^{-8}$	$6.12e^{+2}$	0.54
2-2504	1.01	1.40	1.58	1.40	$0.42e^{-5}$	$1.55e^{-8}$	$2.71e^{+2}$	0.53
2-2765	0.68	0.95	1.35	1.18	$0.22e^{-4}$	$1.19e^{-5}$	1.85	0.30
2-2766	0.89	1.23	1.37	1.21	$1.75e^{-5}$	$0.52e^{-5}$	3.37	0.33
2-2767	0.76	1.05	1.45	1.27	$0.44e^{-5}$	$0.21e^{-6}$	$2.10e^{+1}$	0.43
2-2768	0.79	1.10	1.45	1.33	$0.8e^{-5}$	$0.44e^{-6}$	$1.82e^{+1}$	0.41
2-2769	0.87	1.21	1.52	1.38	$1.3e^{-5}$	$0.67e^{-6}$	$1.94e^{+1}$	0.42

Note: ** in sample # column indicates polyimide substrate, while * indicates molybdenum coated polyimide substrate.

Correlating the data in Tables 4-3 and 4-4 to Tables 4-2 and 4-1, respectively, the following observations can be made:

1. For the most part, film thickness increases linearly with increasing germane flows. Establishing the growth rate for a given set of parameters allows the process engineer to grow films to a desired thickness.

2. As the amount of Ge being incorporated into the film increases, the E_{04} and E_T values shift to lower values as expected. This is due to the fact that pure Si has a Tauc gap around 1.80 eV, while Ge has a Tauc gap around 1.18 eV. Likewise, as the amount of Si is increased into the film, the E_{04} and E_T values shift to higher values as expected.

3. Comparing the E_{04} and E_T values for the depositions at different pressures reveals that they are pressure independent. They do not provide meaningful information into structural differences in the material. However, if one examines the spectrophotometer raw data, i.e. α vs. E and $(\alpha E)^{1/2}$ vs. E plots, one can locate the regions of tail and mid-gap states. An example of these plots is shown in Figure 4-1.

4. The samples deposited at 10 mTorr have lower conductivities than films deposited at 5 mTorr. However, the photo sensitivities of the films deposited at 10 mTorr are larger. This information indicates that there are structural differences between the materials deposited at 5 mTorr and 10 mTorr. As stated before, high dark conductivities and smaller photo sensitivities are signatures of crystallinity.

5. Activation energy data shows that films deposited at 10 mTorr typically have higher energies than their 5 mTorr counterparts. However, in some cases they are similarly high. Also, the silane to germane ratio affects the activation energy. Around a 1.5:1 silane to germane ratio the activation energy peaks due to an amorphous alloy being formed. When silane dominates the ratio, the activation energy corresponds to a micro-crystalline material; however, when germane
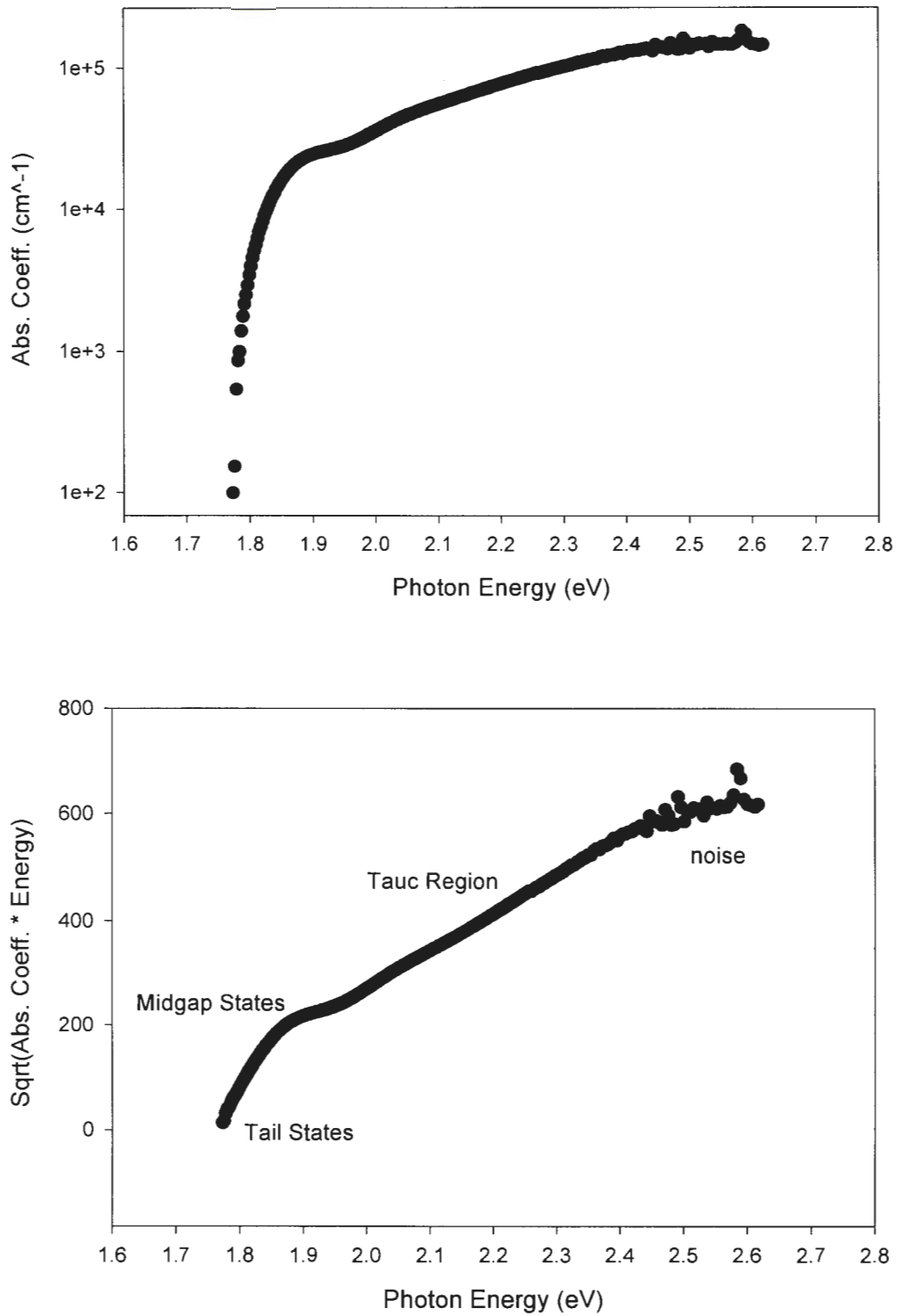
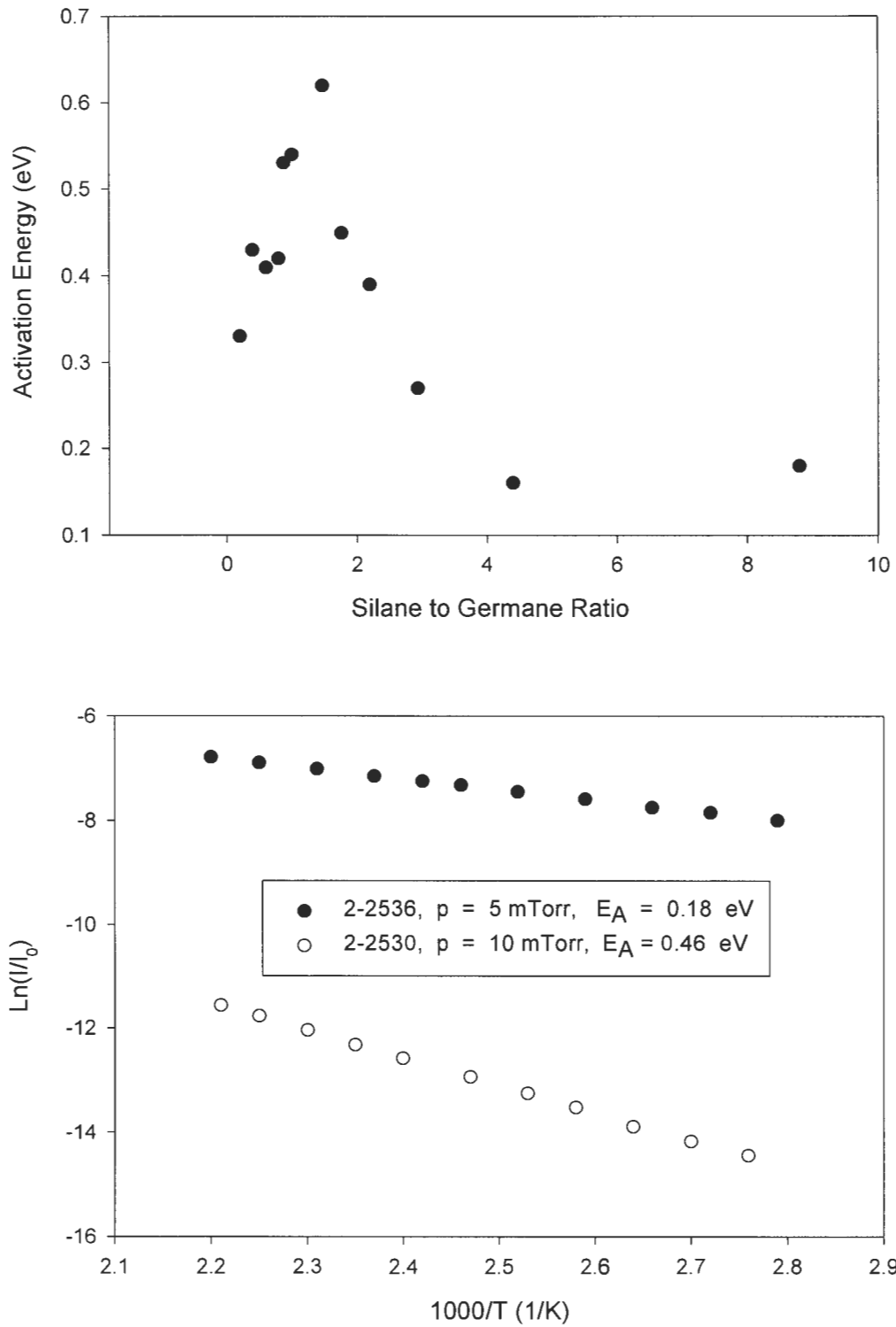Figure 4-1. Spectrophotometer absorption coefficient data and Tauc plot.

Figure 4-2. Representative activation energy data.

dominates the ratio, the activation energy corresponds to an amorphous film. A plot of the gas flow ratio effects and a comparison of activation energies at different pressures are shown in Figure 4-2. As stated before, low activation energies are a signature of crystallinity. Thus, this data substantiates the theory that films deposited at lower pressures are more likely to grow with some degree of crystallinity.

Figures 4-3 through 4-6 show sub-gap absorption data for a number of the samples listed in the tables above. The samples were measured using the two-beam photo conductivity technique. More specifically, Figure 4-3 shows how the shape of the curve is affected by increased amounts of Ge content when deposited at 5 mTorr. Notice that the
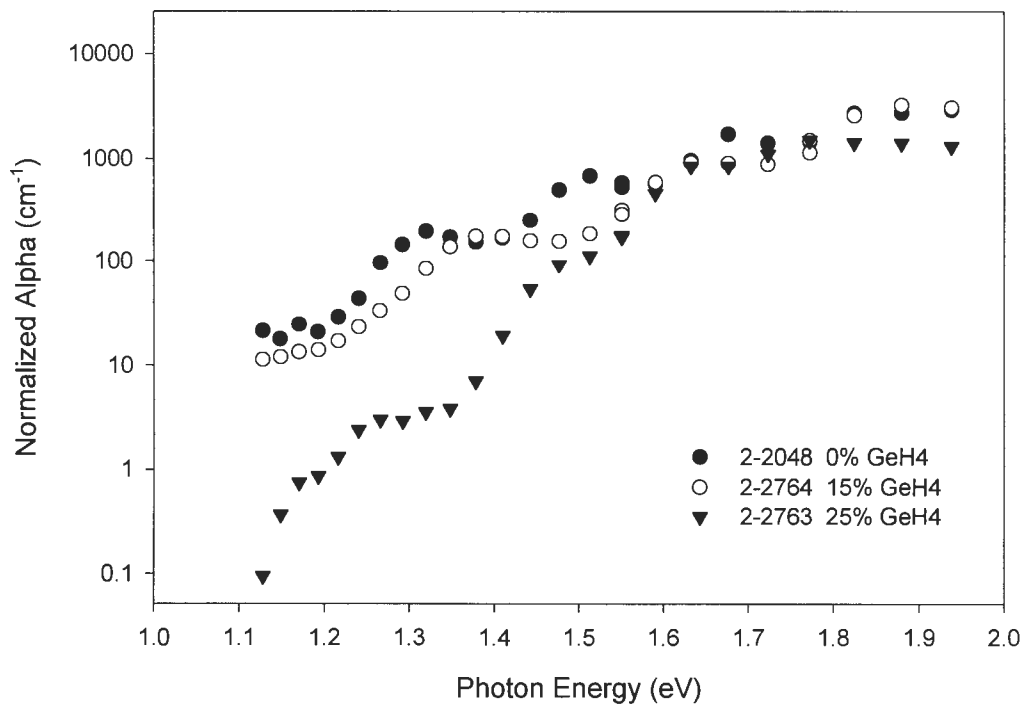
Figure 4-3. Sub-gap absorption for films deposited at 5 mTorr.

2-2048 curve follows that of a rounded micro-crystalline Si:H curve, as reported in Reference [16]. This signature or curve shape predicts that 2-2048 is micro-crystalline. Indeed this prediction is substantiated with Raman data. As Ge content increases, the shape of the curve begins to deviate from the micro-crystalline Si curve. Obviously, this is a result of changing chemical composition in the films. However, what is not obvious is that the structure is changing as well. With 25% germane flow, the shape of the curve is predicting that the film is amorphous.

Figure 4-4 shows sub-gap data for films deposited with 10% GeH$_4$ flow. Based on the curve shapes, it would be a safe guess that the deposition on glass (2-2561) at 5 mTorr has some degree of crystallinity, while the deposition on glass (2-2531) at 10 mTorr is probably amorphous. Note that the deposition on the molybdenum coated polyimide
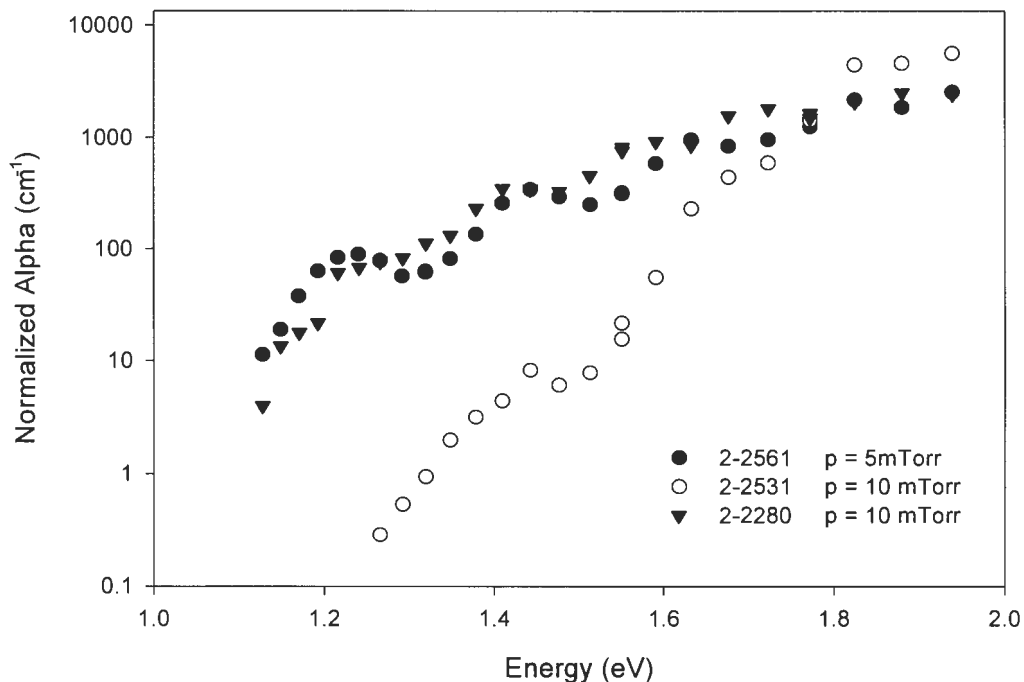

Figure 4-4. Sub-gap absorption for films deposited with 10% GeH$_4$ flow.

substrate (2-2280) probably has some degree of crystallinity, even while deposited at 10 mTorr. This is an important observation.

Similarly, Figure 4-5 shows absorption gap data for films deposited with 20% GeH$_4$ flow. Again the film deposited at 5 mTorr on the molybdenum coated substrate (2-2311) shows some degree of crystallinity as does the film on the glass substrate (2-2506).

Figure 4-6 contains information on the films deposited with 30% GeH$_4$ flow. In this case, the films are probably amorphous regardless of the deposition pressure.

Thus, these four figures show that the GeH$_4$ flow, i.e., SiH$_4$ to GeH$_4$ ratio, and the chamber pressure play a role in determining the structure of the film. Also, a conductive substrate is able to counteract the effect chamber pressure has on the resulting film structure.
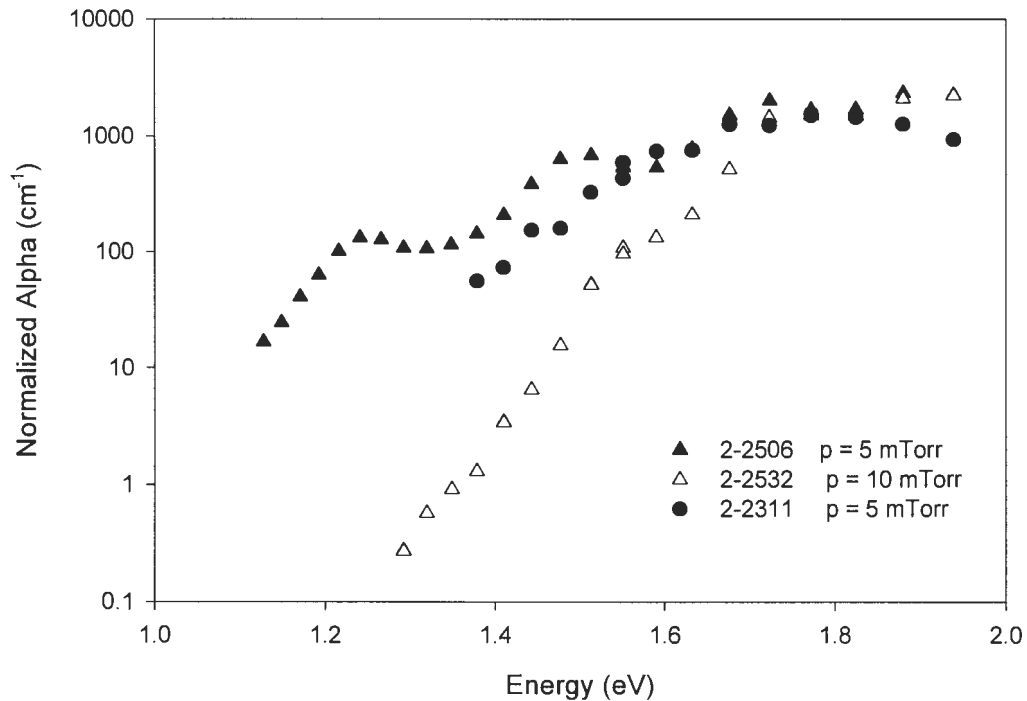

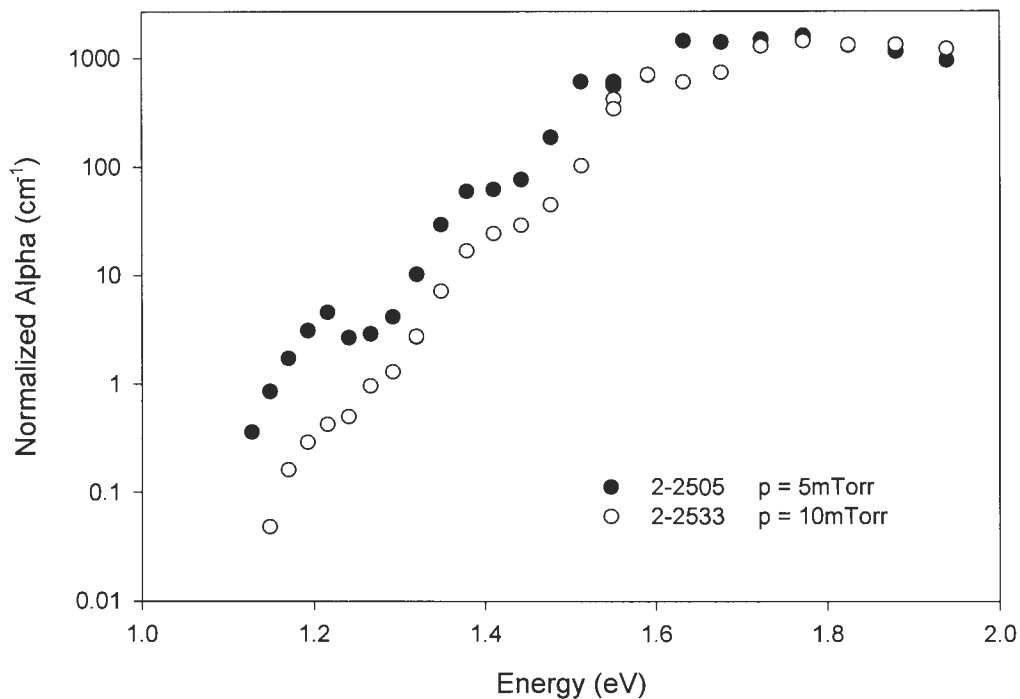Figure 4-5. Sub-gap absorption for films deposited with 20% GeH$_4$ flow.

Figure 4-6. Sub-gap absorption for films deposited with 30% GeH$_4$ flow.

To truly determine the structure of the films, Raman spectroscopy measurements are performed. Figures 4-7 through 4-15 show the Raman spectra of the (Si,Ge) films corresponding to the sub-gap absorption data presented in the previous four figures. As expected, the Raman spectra for 2-2048, a film produced using SiH$_4$ and H$_2$, showed a sharp peak at 520 cm^{-1}. Incorporating more germanium into the silicon film causes this peak to shift to lower wavenumbers. Meanwhile, a germanium peak begins to form. The figures presented on the next few pages map the structural content of the (Si,Ge) alloys with increasing amounts of germane flow. The samples in the Figures 4-7 to 4-11 are deposited with a vacuum pressure of 5 mTorr, while the samples in Figures 4-12 to 4-15 are deposited at 10 mTorr.

At a silane to germane ratio of 4.4:1, a second peak begins to form around 400 cm^{-1} (see Figure 4-7). This second peak corresponds to a Si - Ge mode. There is probably not enough Ge in the film to produce a Ge - Ge peak. Since the Si - Si mode is very strong, the material behaves as if it is micro-crystalline. Indeed, the sub-gap absorption and activation energy data for this film agree with this finding.
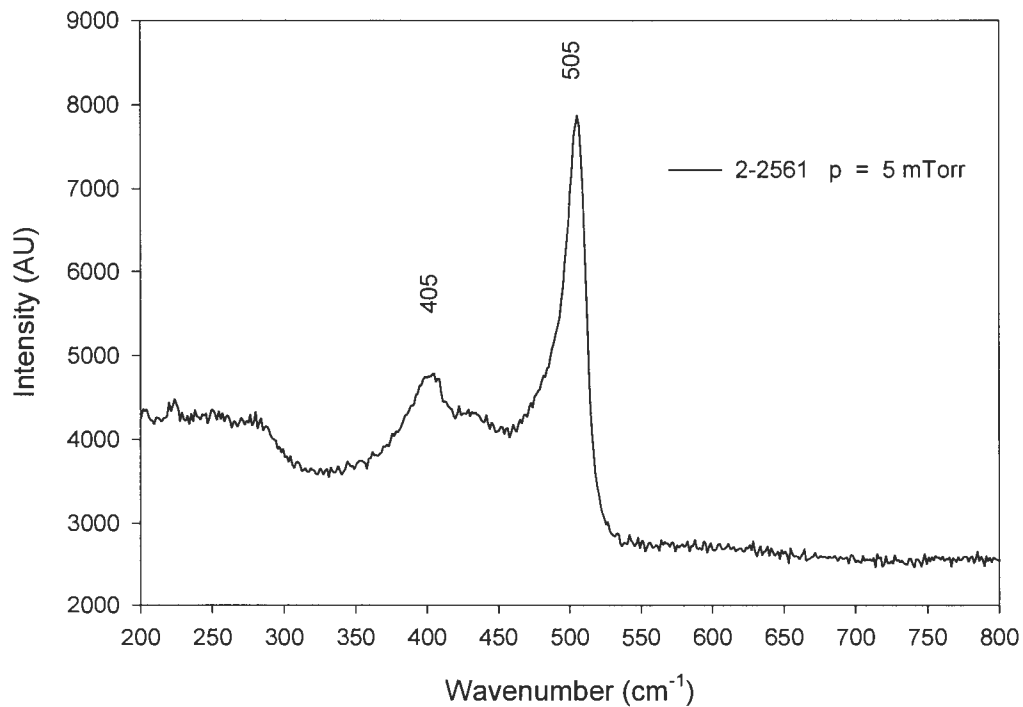

Figure 4-7. Raman spectrum of a 5 mTorr deposition on 7059 glass with 10% GeH$_4$ flow.

At a silane to germane ratio of 2.93:1, all three peaks are noticeable (see Figure 4-8). The Si - Si peak is still sharp; however, its strength is reduced due to the other peaks growing stronger with the increased presence of Ge. All of the characterization data on the behavior of this film leads to the conclusion that the material exhibits a micro-crystalline structure.
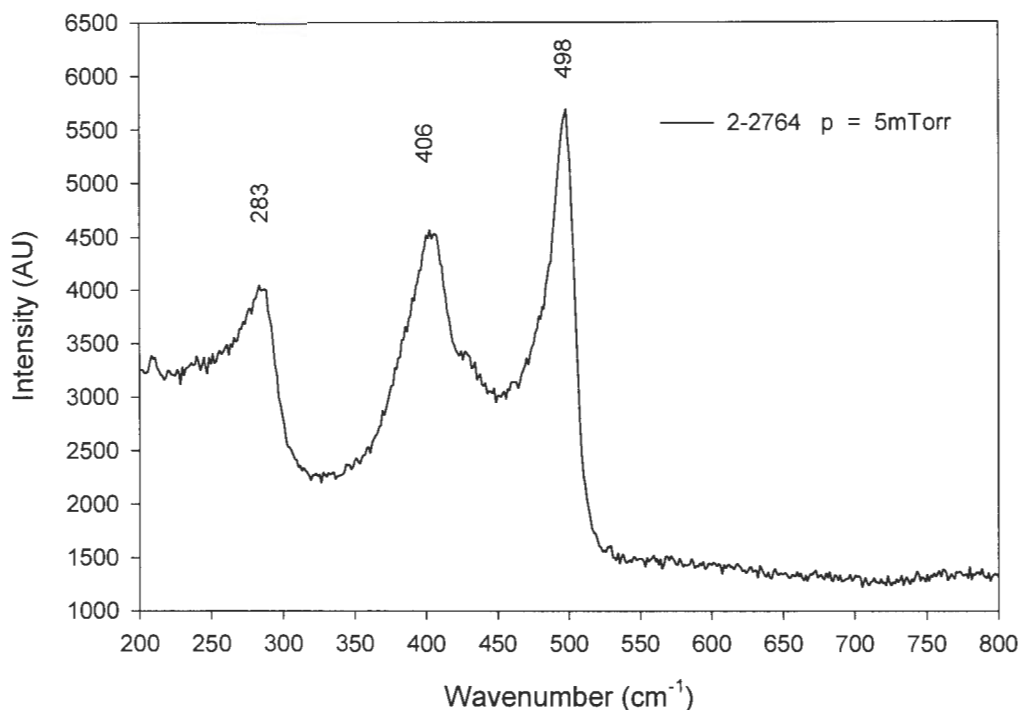
Figure 4-8. Raman spectrum of a 5 mTorr deposition on 7059 glass with 15% GeH$_4$ flow.

At a silane to germane ratio of 2.2:1, there are clearly 3 sharp peaks with almost equivalent strengths (see Figure 4-9). A similar result is obtained for the film (2-2311) deposited on molybdenum coated polyimide. The Ge - Ge mode, 288 cm^{-1}, is shifted to a higher value, while the Si - Si mode, 494 cm^{-1}, is shifted to a lower value. The center peak is a Si - Ge mode, 406 cm^{-1}. The data obtained in this figure are similar to that presented by Ganguly and co-workers [23]. Their films are deposited in a RF parallel plate reactor. Thus, this result is an intrinsic property of the material and not just a result of the processing technique.
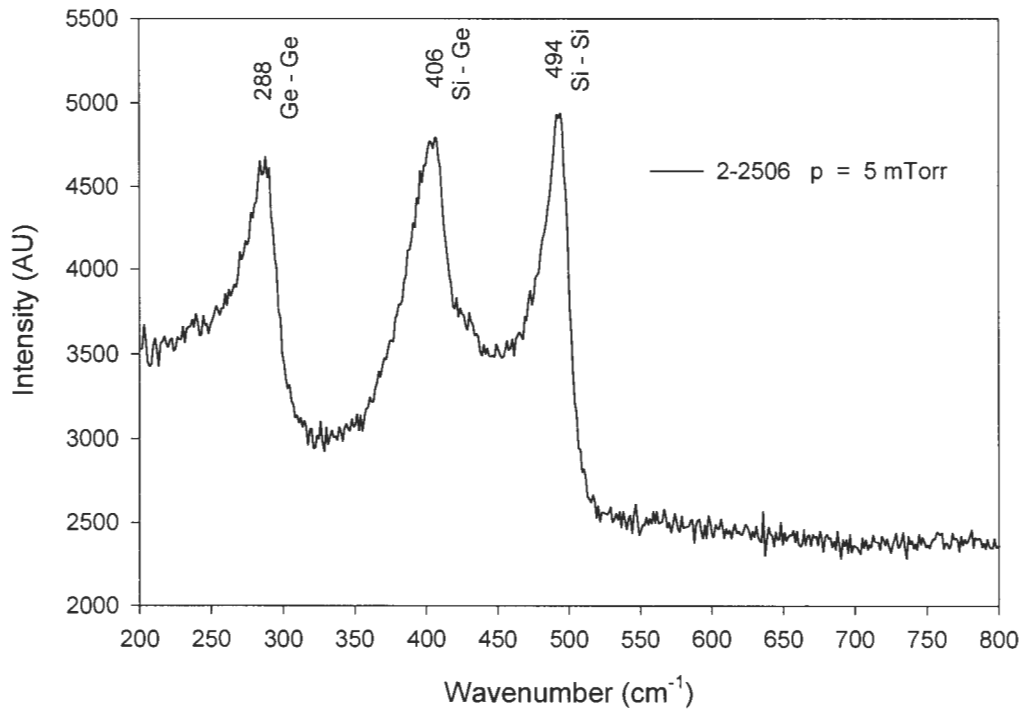
Figure 4-9. Raman spectrum of a 5 mTorr deposition on 7059 glass with 20% GeH$_4$ flow.

At a silane to germane ratio of 1.76:1, the material becomes amorphous (see Figure 4-10). The Si - Si mode nearly disappears, while the Si - Ge and Ge - Ge modes significantly broaden. This result is unexpected based on the previous trend of results. However, comparing this information with the sub-gap absorption data and the activation energy value, this result should not be a surprise as the signatures of the other measurements were predicting an amorphous material.

At a silane to germane ratio of 1.475:1, the material is clearly amorphous (see Figure 4-11). Similar results are obtained for subsequent decreasing of the silane to germane ratio. As the amount of Si in the film is reduced the Si - Ge peak disappears and the Ge - Ge peak
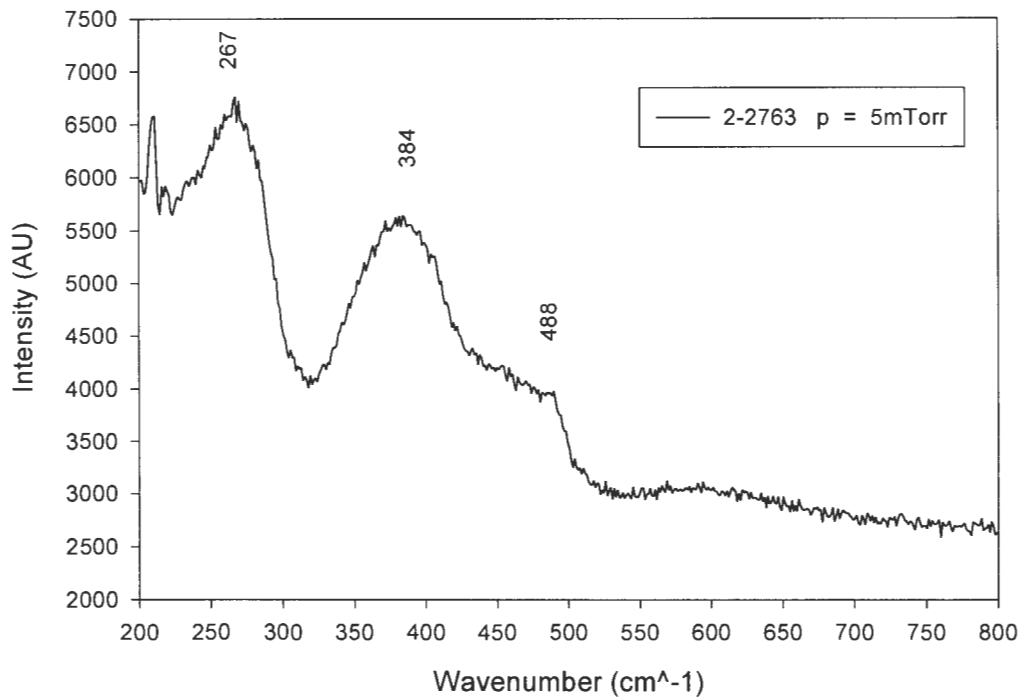
Figure 4-10. Raman spectrum of a 5 mTorr deposition on 7059 glass with 25% GeH$_4$ flow.
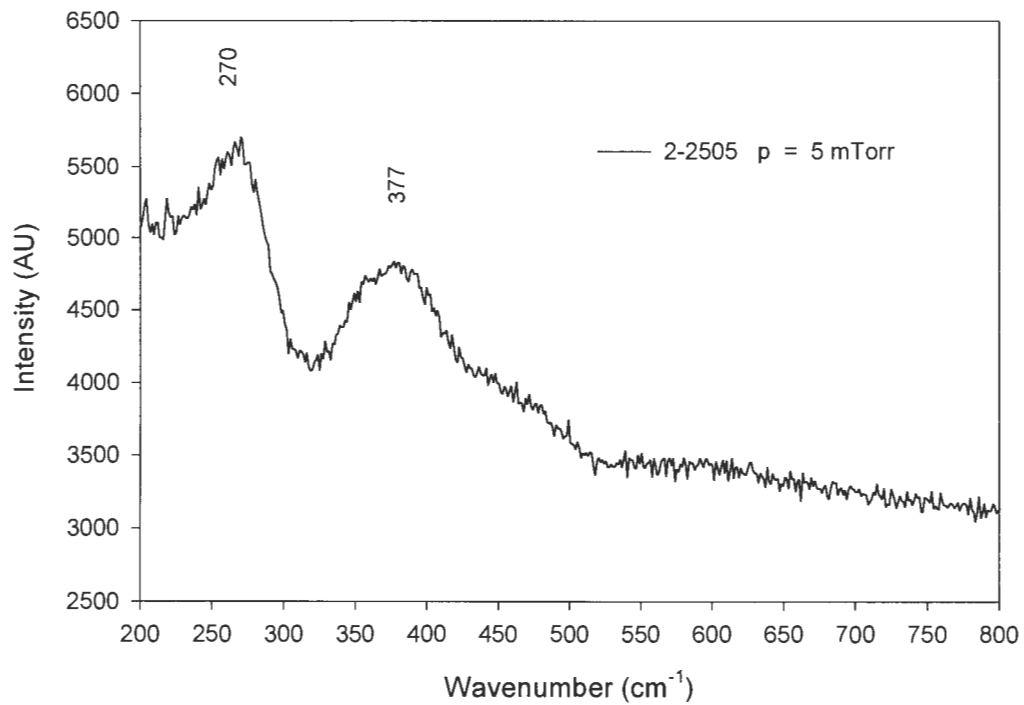

Figure 4-11. Raman spectrum of a 5 mTorr deposition on 7059 glass with 30% GeH$_4$ flow.

grows stronger. Unfortunately, a 40:1 hydrogen to germane ratio does not create a micro-crystalline peak like a similar hydrogen and silane combination that is deposited on 7059 Corning glass. Perhaps finding the "magic" hydrogen to germane ratio and mixing it with the appropriate amount of silane will lead to a better micro-crystalline material.

The only difference between the data presented in Figure 4-12 and the data presented in Figure 4-7 are that the films are deposited at different vacuum pressures. Clearly, the 10 mTorr pressure results in an amorphous film. This is due to the decreased amounts of hydrogen and ion bombardment during the growth as shown in Figure 2-3.
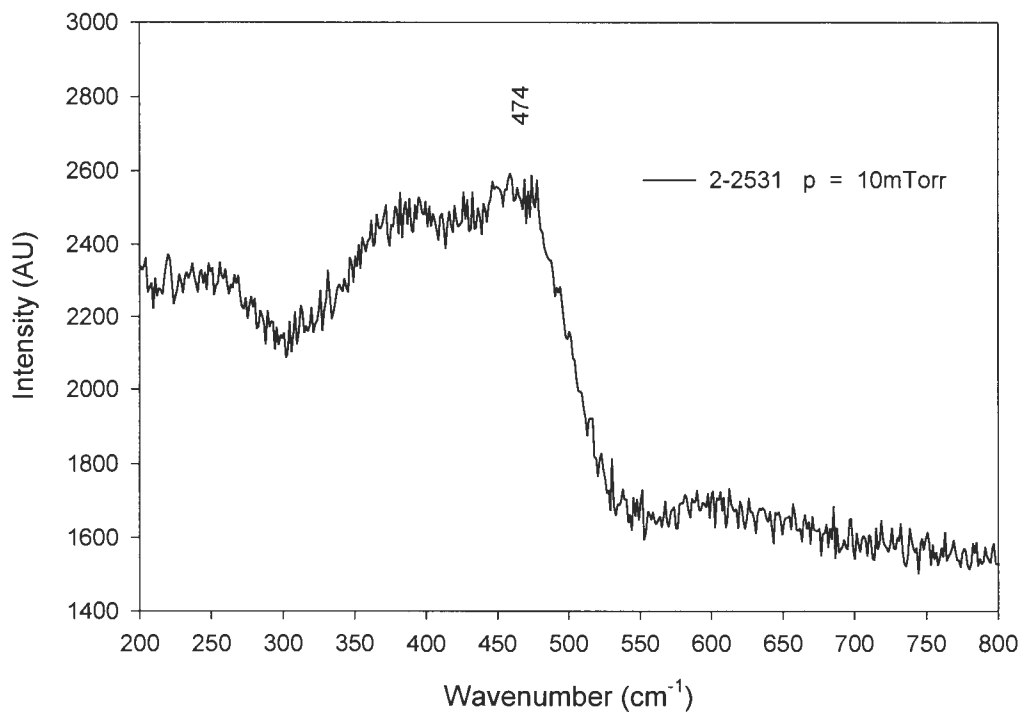

Figure 4-12. Raman spectrum of a 10 mTorr deposition on 7059 glass with 10% GeH_4 flow.

The only difference between Figure 4-13 and 4-12 is that the substrates are different. Clearly, the film deposited on molybdenum coated polyimide is micro-crystalline even at 10 mTorr. The difference can be accounted by the fact that the substrate is conductive instead of insulating. This results in the conductive substrate being set to the same potential as the chamber walls, which are grounded. Thus, the potential that the ions and radicals see is essentially the same during the growth process. For insulating substrates a charge builds up and begins to repel the incident ion flux. Perhaps biasing the substrate would eliminate this problem. This result shows the importance of ions in promoting micro-crystallinity.
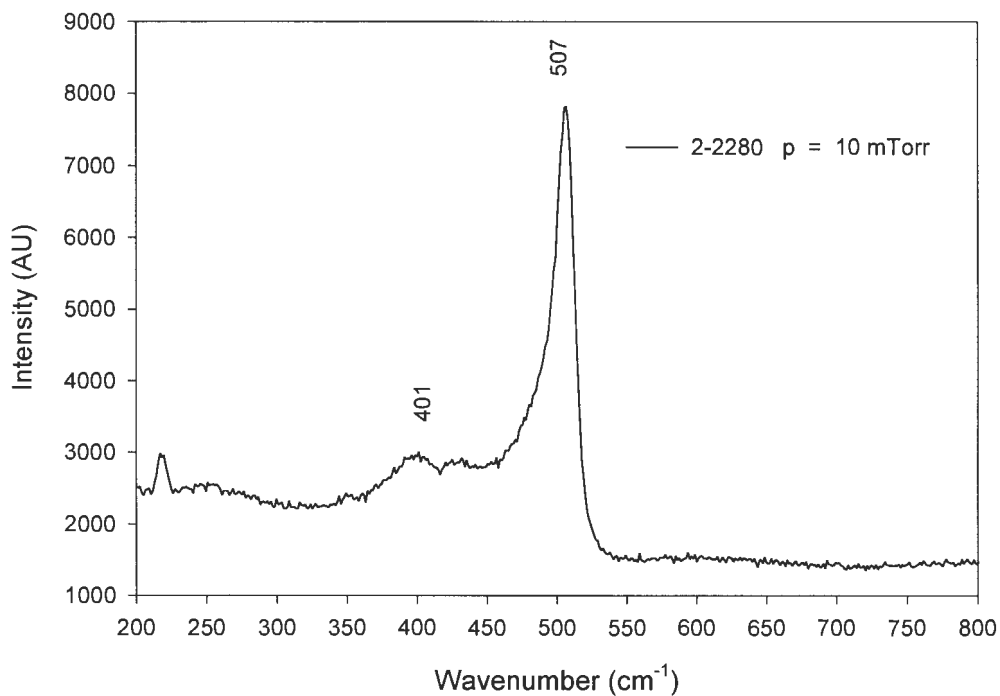

Figure 4-13. Raman spectrum of a 10 mTorr deposition on molybdenum coated polyimide with 10% GeH_4 flow.

The data in Figure 4-14 are similar to the data in Figure 4-8 with the exception that the films are deposited at different pressures. Clearly, the higher pressure film (Figure 4-14) is amorphous and contains a broad Si - Ge peak. At this silane to germane ratio, the Ge -Ge mode is not yet noticeable when the deposition is performed at 10 mTorr.
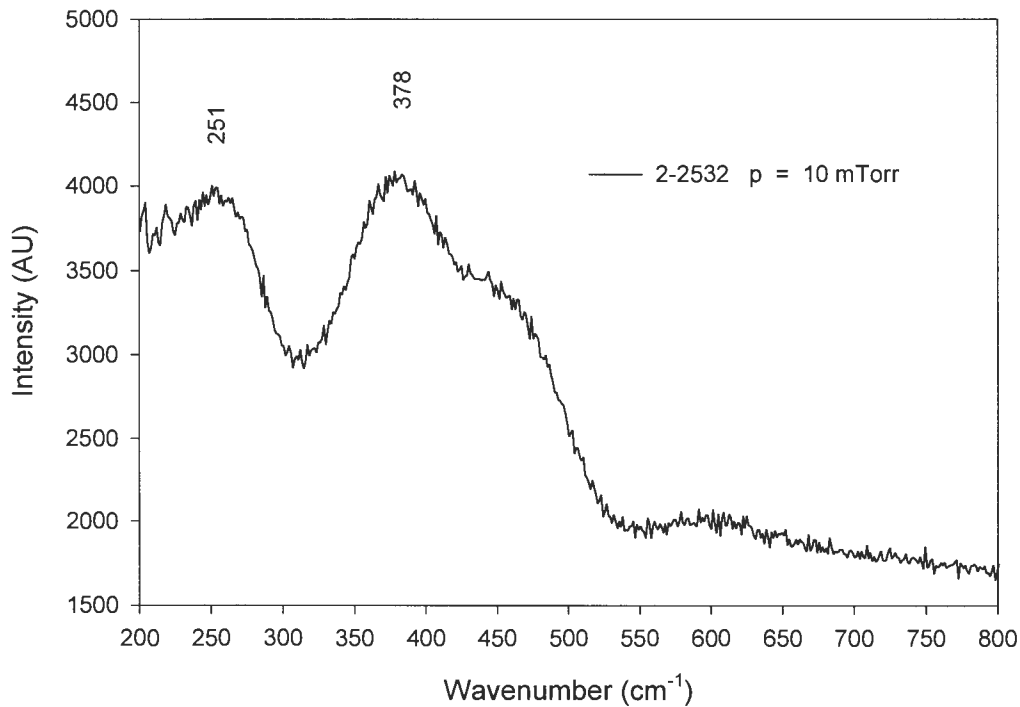

Figure 4-14. Raman spectrum of a 10 mTorr deposition on 7059 glass with 20% GeH$_4$ flow.

In Figure 4-15, the material is amorphous, i.e., the peaks are broad. The Ge - Ge mode is now noticeable. Analysis of results obtained by further decreasing the silane to germane ratio yield a similar conclusion.

The major problem involving analysis of (Si:C) alloys is that the material fluoresces at the laser wavelength used in the Raman apparatus resulting in a swamped signal. Other
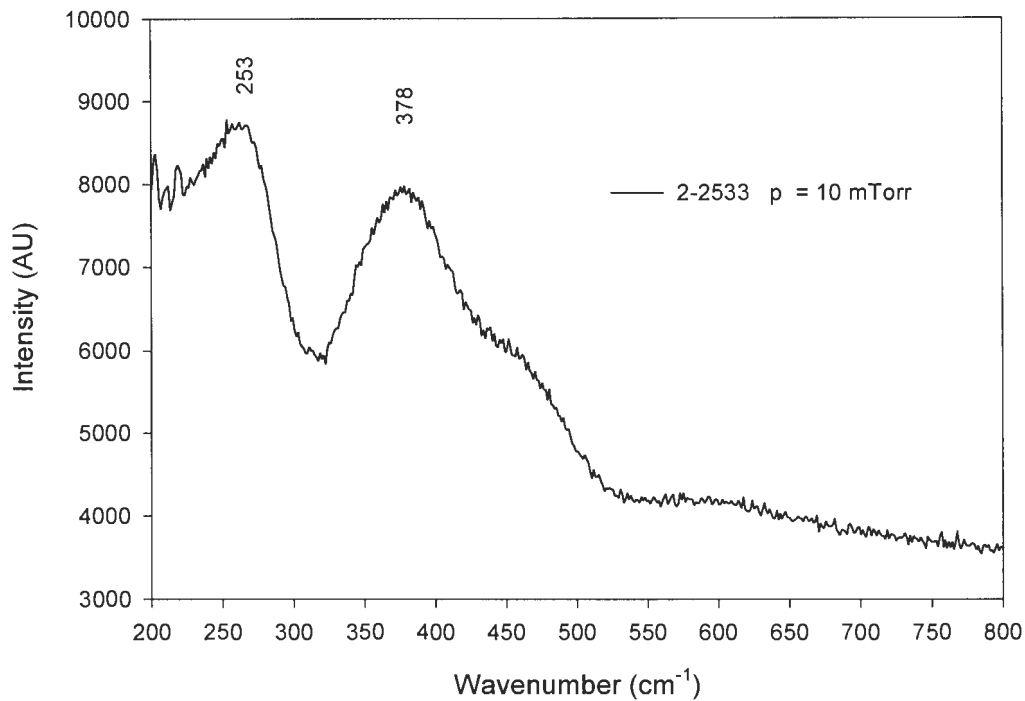
Figure 4-15. Raman spectrum of a 10 mTorr deposition on 7059 glass with 30% GeH$_4$ flow.

wavelength lasers might be able to overcome this problem, but we do not have access to them. Another problem that exists is that the material is innately insulating. Electrical measurements were unable to be obtained even for biases over 100 volts. Without gaining the necessary data, it is impossible to discuss the structure and quality of the material being deposited. Another drawback to working with Si,C films are that the growth rates are extremely low. Deposition times to grow one micron of material are about six hours. Perhaps, increased ion bombardment would help in growing micro-crystalline (Si:C) films. This is a potential subject for future research.

In summary, the data presented in this chapter shows that the Raman spectra verifies the assumptions made about the activation energy, conductivity, and sub-gap absorption

structural signatures. Also, the data clearly shows that gas flow ratio and the type of substrate play a major role in determining the structural properties of the deposited material.

CHAPTER 5. CONCLUSIONS

The objective behind developing micro-crystalline (Si:Ge):H and (Si:C):H films are to use these materials to make better of solar cells. The higher absorption coefficients of these materials compared to micro-crystalline silicon over the solar spectrum make it an attractive alternative bottom cell material [23].

Process parameters have been determined that lead to high quality micro-crystalline (Si,Ge):H films deposited at temperatures below 300 °C using a plasma generated by electron cyclotron resonance conditions. Unfortunately, similar experiments on depositing (Si:C):H films were not successful. Characterization of these films involved measuring the activation energy, photo and dark conductivities, spectrophotometer and sub-gap absorption, and Raman scattering spectra. Using this analysis, we are able to correlate the resulting film structure with the process parameters. Also, we have determined structural signatures for the characterization measurements so that Raman analysis need not be performed on all samples. These micro-crystalline signatures are low activation energies, high photo and dark conductivities, and a rounded sub-gap absorption curve between 1 and 2 eV. The Raman analysis substantiates these signatures.

In order to obtain micro-crystalline growth two things must happen. First, the deposition conditions must lead to significant ion bombardment of the substrate. This means using a combination of high power and low pressure. A conductive/insulating substrate also plays a role in determining the structure. We determined that use of a conductive substrate allows for micro-crystalline growth at higher pressures than an insulating substrate. Also, we were unable to grow micro-crystalline structures on polyimide substrates under conditions

that resulted in micro-crystalline structures forming on glass substrates. Along with the substrate charging, we believe there are atomic scale chemical reactions between the substrate and depositing radicals that prevent the creation of micro-crystalline films on polyimide. This chemistry interface is something that we do not understand. For further information into polyimide materials the reader should check the work performed by Ghosh and Mittal [24]. Second, the plasma chemistry and the precursor gases, silane and germane, must be mixed in the proper ratio. The Raman spectroscopy data clearly shows the structural changes in (Si,Ge):H alloys as the ratio is varied from mostly Si to mostly Ge films.

Using the spectrophotometer data we were able to see the Tauc and E_{04} gaps shift within the bounds of pure silicon and germanium films. These plots also provide insight into the amount of mid-gap and defect states in the material. It was also determined that the film thickness varies linearly with increased amounts of gas rate flow. The film's quality may also be ascertained by the amount of noise in the measured signal when performing activation energy, conductivity, and sub-gap absorption measurements.

Thus, we have established both measurement techniques and process parameters that lead to high quality micro-crystalline (Si:Ge):H films deposited at low temperatures. Future work in this area could include biasing the substrate to determine its effect on the structure of the deposited film. Also, more experiments should be performed to determine the low temperature conditions that lead to good micro-crystalline (Si,C):H alloys.

APPENDIX A. ELECTRON MOTION IN A STATIC MAGNETIC FIELD

The motion of free electrons in the plasma generation region are governed by the Lorentz force,

$$F = q\left(v \times B\right). \tag{A-1}$$

This causes the electrons to spiral around the direction of the static magnetic field. If we assume the magnetic field is in the z direction, i.e. $B = B_0\, a_z$, Equation (A-1) can be expressed as

$$m\left(\frac{d^2x}{dt^2}a_x + \frac{d^2y}{dt^2}a_y + \frac{d^2z}{dt^2}a_z\right) = q\,B_o\left(v_y\,a_x - v_x\,a_y\right). \tag{A-2}$$

Equating components yields three separated second order differential equations.

$$m\frac{d^2x}{dt^2} = q\,B_o\,v_y, \qquad m\frac{d^2y}{dt^2} = q\,B_o\,v_x, \qquad m\frac{d^2z}{dt^2} = 0 \tag{A-3}$$

Integrating the above equations with respect to t yields

$$\frac{dx}{dt} = \frac{q\,B_o\,y}{m} + C_1, \qquad \frac{dy}{dt} = -\frac{q\,B_o\,x}{m} + C_2, \qquad \frac{dz}{dt} = C_3. \tag{A-4}$$

Substituting the results in Equation (A-4) into Equation (A-3) will lead to differential equations in terms of position. For example, the equation of motion in the x direction is

$$\frac{d^2x}{dt^2} + \omega_o^2\,x = x_o\,\omega_o \tag{A-5}$$

where $\omega_0 = qB_0/m$ and $x_o = C_2/m\,\omega_0$. The solution to this equation is of the form

$$x = x_0 + R\,cos(\omega_o t + \delta) \tag{A-6}$$

where R and δ are the constants of integration. Taking the time derivative of Equation (A-6)

yields the x component of the velocity.

$$v_x = -R\,\omega_o sin(\omega_o t + \delta) \tag{A-7}$$

These results can then be substituted into Equation (A-4) to obtain the position and velocity of the electrons in the y direction

$$y = y_0 - R\,sin(\omega_o t + \delta) \tag{A-8}$$

$$v_y = -R\,\omega_o\,cos(\omega_o t + \delta) \tag{A-9}$$

where $y_0 = C_1 / m\,\omega_0$. Equations (A-6) through (A-9) define the motion of electrons in the plane perpendicular to the magnetic field. Squaring and adding Equations (A-6) and (A-8) reveals that the electron motion follows a circular path with radius, R, about the z axis.

$$(x - x_o)^2 + (y - y_o)^2 = R^2 \tag{A-10}$$

Solving for the radius, R, requires the use of Equations (A-7) and (A-9).

$$R = \frac{\sqrt{v_x^2 + v_y^2}}{\omega_o} = \sqrt{v_x^2 + v_y^2}\left(\frac{m}{q\,B_o}\right) \tag{A-11}$$

Since the velocities of the electrons in the z direction are parallel to the magnetic field, i.e. constant, the electrons spiral around the z axis with a frequency of

$$\omega_o = \frac{q\,B_o}{m} \tag{A-12}$$

and a radius given by Equation (A-11).

APPENDIX B. ABSORPTION COEFFICIENT MATCHING

To match the sub-gap and spectrophotometric absorption coefficient measurements,

we have to be aware of the approximations used in obtaining α_{subgap}.

We are assuming that sub-gap photo conductivity is proportional to the number of

absorbed photons. The number of absorbed photons, N_{abs}, is given by

$$N_{abs} = 1 - e^{-\alpha t} \qquad\qquad (B\text{-}1)$$

where t is the thickness of the film. This approximation is valid for regions of photon energy

where α is less than 10^2 cm^{-1} and $N_{abs} = \alpha t$. However, in spectrophotometric measurements,

this approximation is not valid because the αt product becomes much larger than the number

of absorbed photons. Thus, we have to make a correction for α_{subgap} photo conductivity

measurements to appropriately match the different types of absorption coefficients.

Combining the absorption coefficients provides detailed information about the defect states

around the Fermi energy. The procedure to determine the correction factor is as follows:

1. Determine α using the spectrophotometer measurements. Typically, α will be in

     the range of 10^3 to 10^5 cm^{-1} and αt may be 0.2 to 0.5. Call this α_R for real α.

2. Calculate the photo conductivity, α_{pc}, using the relationship

$$\alpha_{pc} = \frac{1 - e^{-\alpha_R t}}{t} \qquad\qquad (B\text{-}2)$$

This calculation converts the spectrophotometric, α_R, to the α being measured in

the sub-gap regime when α is very small.

3. Matching the α_{subgap} curve to the α_{pc} curve is achieved by comparing the two α values at the same photon energy. From this comparison it is possible to determine a multiplier factor. This comparison should be done at several photon energies to reduce calibration errors and should give the correct multiplier factor for the sub-gap curve.

Note that the correction factors will be different for different photon energies because of the non-small αt for energies greater than 1.75 eV. However, only one multiplier factor for the low energy photo conductivity curve should result if the measurements are made carefully and the above procedure is applied correctly.

APPENDIX C. GROWTH OF MICRO-CRYSTALLINE SI:H AND (SI,GE):H ON POLYIMIDE SUBSTRATES USING ECR DEPOSITION TECHNIQUES

KARL ERICKSON*, VIKRAM L. DALAL* AND GEORGE CHUMANOV+
*Dept. of Electrical and Computer Engineering
+ Dept. of Chemistry
Iowa State University, Ames, Iowa 50011, USA

ABSTRACT

We report on the growth of good quality micro-crystalline Si:H and (Si,Ge):H films on polyimide substrates using a remote plasma ECR deposition technique. We find that under conditions that lead to significant ion bombardment of the substrate, the films are micro-crystalline even at relatively low deposition temperatures of about 250 C. A critical factor in inducing micro-crystallinity is the presence of a metal coating layer on polyimide. In the absence of such a coating, the films are amorphous, probably because the uncoated polyimide substrate charges up and prevents any further ion bombardment. The quality of the films was measured using both Raman spectroscopy and by studying the activation energy and low-energy absorption coefficient of the films. The sub gap absorption coefficient was found to follow the crystalline Si absorption curve quite well. The addition of germane to the gas phase shifted the absorption curve to smaller energies.

INTRODUCTION

Micro-crystalline(μc) group IV alloys are of significant interest for many device applications. Examples are thin film transistors [1], emitter junctions for bipolar transistors [2],

solar cells [3] and imaging devices in which the light absorption is by an amorphous material, but the carrier transport is through micro or poly-crystalline materials. A number of groups have recently reported the growth of high quality micro-crystalline Si alloys, using either the VHF glow discharge deposition techniques [4], or the low pressure ECR growth technique [5]. Most of this work has been on glass, or glass coated with a transparent conductor, substrates. However, it would be useful to be able to deposit undoped micro-crystalline films on a plastic substrate, for applications such as large area TFT-based memory devices [6], or flexible display and solar cell devices [7]. In this paper, we report on the growth of high quality micro-crystalline Si and (Si,Ge) alloys using the remote ECR technique [8].

GROWTH TECHNIQUE

The basic growth technique is to use an ECR plasma reactor in a remote, reactive mode. In this technique [8], a beam of H ions and radicals, generated by an intense ECR plasma source, is directed towards the substrate in a line of sight fashion, see Fig. 1. The resonance zone of the plasma is about 30 cm away from the substrate, and can be changed using the two magnets, which provide the field necessary for achieving the ECR condition. The precursor gases such as Silane are introduced near the substrate. The pressure in the reactor is kept low, so as to allow for a significant flux of H radicals and ions to reach the substrate. Near the substrate, the electrons in the plasma, and the H radicals, react with Silane, producing primarily the SiH_3 radical, which then leads to the growth of Si films. As the pressure in the reactor is reduced, the energy, and the flux, of H ions increases, see Fig. 2. Therefore, at low pressures, the growing film is subjected to increased ion bombardment and to increased etching due to H
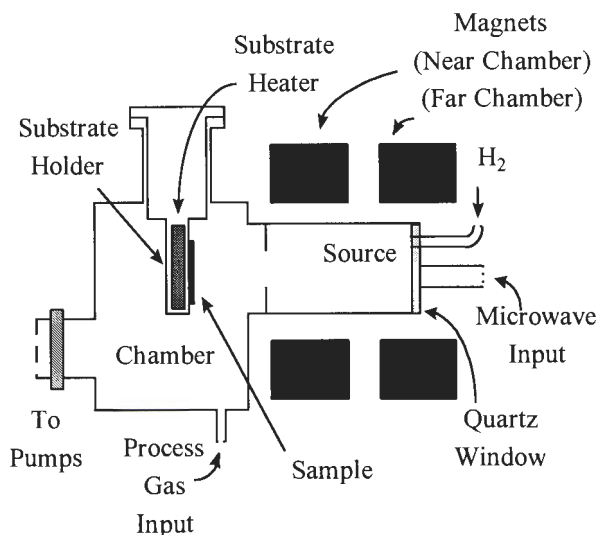
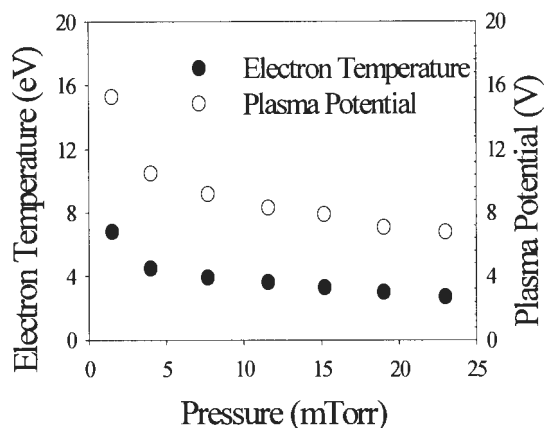Fig. 1. Diagram of the ECR System.

Fig. 2. Plasma potential in H-ECR
discharge as a function of pressure
and power.

radicals. The combination of etching-during-growth [9], and the ion bombardment by reactive

ions, can be expected to lead to improvements in crystallinity [9].

The substrates were either polyimide, or polyimide coated with a thin layer of

Molybdenum. The substrates were maintained at a temperature of about 250-260 C by an

external heater. The typical growth conditions are listed in Table I below.

Table I: Growth Conditions

H_2 flow rate :	40 sccm
Silane flow rate :	1-2 sccm
Pressure :	5 mTorr
Power :	200 W

The typical thicknesses of the films were in the range of 0.8-1.0 μm, with the (Si,Ge)

film, which was made using a mixture of germane and Silane, also under high H_2 dilution,

being slightly thinner (0.65 μm). The typical growth rates were in the range of 1 A/sec.

RESULTS

In Fig. 3, we show the Raman spectrum of two μc-Si:H films deposited on Mo-coated polyimide substrates. Quite clearly, the films show a Raman peak characteristic of a poly-crystalline material. The sharp peak in the left plot occurs at 514 cm^{-1}, while the peak in the right plot occurs at 513 cm^{-1}.
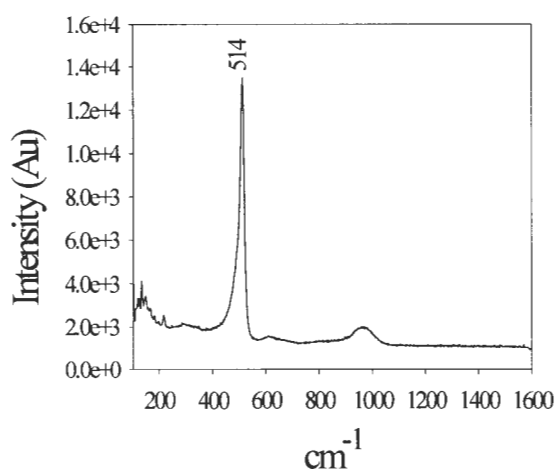

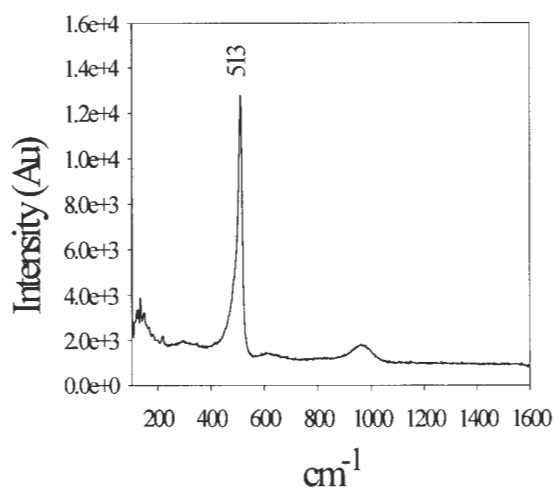Fig.3a. The Raman scattering spectrum of a μc-Si:H film grown on a Mo-coated polyimide substrate.

Fig.3b. A Raman scattering spectrum of a μc-Si:H film grown on a Mo-coated polyimide substrate under slightly different deposition conditions.

In Fig. 4, we show the Raman spectrum for a film deposited on an uncoated polyimide substrate. The film shows only a broad peak characteristic of a-Si:H, even though the deposition conditions were otherwise identical to the ones whose spectra is shown in Fig. 3. In Fig. 5, we show the Raman spectrum for a micro-crystalline (Si,Ge):H film, also deposited on a Mo-coated polyimide substrate. There is a sharp peak at 507 cm^{-1}, characteristic of a Si line. In addition, there seems to be another peak at about 396 cm^{-1}, which may be a Ge peak.
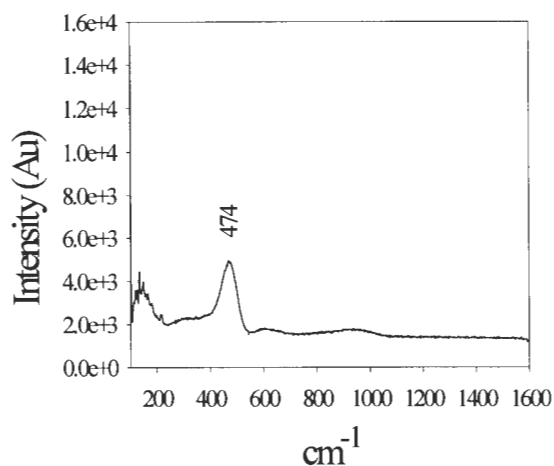
Fig. 4. The Raman scattering spectrum of an a-Si:H film grown on a polyimide substrate.
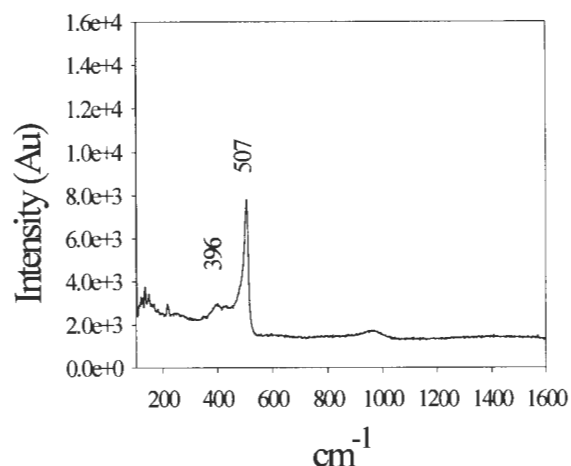
Fig. 5. The Raman scattering spectrum of a μc-(Si,Ge):H film grown on a Mo-coated polyimide substrate.

To confirm that the films were indeed micro-crystalline or amorphous, we measured the absorption spectra for these films using a two-beam photo-conductivity technique [10]. In this technique, one uses a dc light beam of low intensity to fix the quasi Fermi levels(and hence carrier lifetimes), and then probes the photo-conductivity of the sample using a second ac light beam. The absorption coefficients so determined for an a-Si:H, and two μc-Si:H, and one μc-(Si,Ge):H film are plotted in Fig. 6. The absorption curves for Si were normalized to the c-Si absorption curve at 1.5 eV, and are found to follow the absorption curve for c-Si quite well down to 1.17 eV. We don't accurately know the Ge composition of our (Si,Ge):H sample, and therefore, we decided to arbitrarily match the absorption again at 1.5 eV to c-Si absorption curve. Since we are on a metallized substrate, we cannot measure absorption directly. Upon examination of Fig. 6, we see that the curve for μc-(Si,Ge):H seems to follow the μc-Si curve,

but is shifted to a lower energy compared with the curve for μc-Si, thus confirming the micro-crystalline nature of the material.

To further confirm that the materials were micro-crystalline or amorphous, we measured the conductivity activation energy, using a sandwich geometry on the metallized substrates, and coplanar on the uncoated polyimide. In Fig. 7, we show the results of activation energy measurements on the micro-crystalline and amorphous materials. The materials which were confirmed to be micro-crystalline from Raman and absorption measurements have very small activation energies, whereas the materials which show the amorphous Raman spectrum and absorption curve have much larger activation energies.
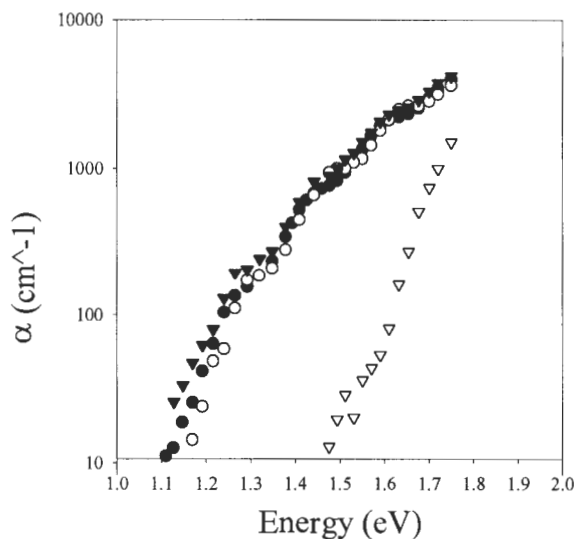

Fig. 6. Sub gap absorption coefficients for a-Si:H(∇), μc-Si:H(● Fig.3a, ○ Fig.3b), and μc-(Si,Ge):H(▼) grown on Mo-coated polyimide substrates.
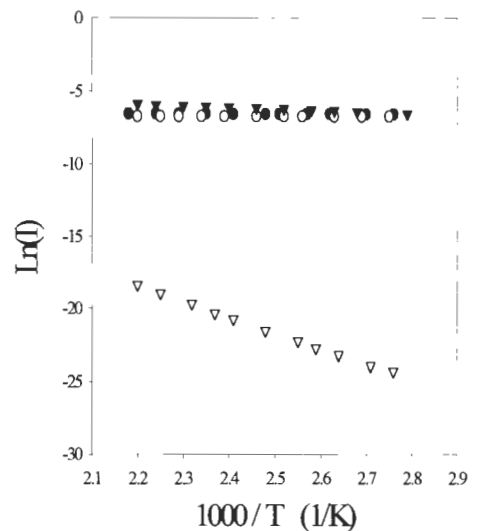
Fig. 7. Activation energy for a-Si:H(∇ with E_A = 0.92 eV), μc-Si:H(● Fig.3a with E_A = 0.01 eV, ○ Fig.3b with E_A = 0.00 eV), and μc-(Si,Ge):H(▼ with E_A = 0.10 eV).

We have also measured the influence of pressure on the formation of micro-crystalline films. We find that even on metallized substrates, a high pressure growth(10 mTorr) leads to

58

the formation of amorphous phase, whereas a reduction in pressure leads to the onset of micro-crystallinity. In Fig. 6, we have shown the absorption curve of a film deposited at 10 mTorr pressure, clearly showing the amorphous absorption spectrum.

DISCUSSION

We have shown that one needs a metallized substrate to be able to achieve micro-crystallinity under our conditions. This is a surprising result, since, in general, one has surplus of H radicals present at the surface during growth. Such H radicals must be causing some etching-during-growth, which should help in nucleating the crystalline phase, by etching away the amorphous bonds. A metallized substrate, in contrast to an uncoated substrate, is subjected to the effects of a high flux of H ions during growth. Therefore, we conclude that the H ion bombardment has something to do with achieving micro-crystalline phase, at least in an ECR system. This conclusion is supported by the observation that, to achieve micro-crystallinity, one has to lower pressures, which leads to more reactive ion bombardment during growth. This conclusion is similar to the one reached by Dalal et al, during their pioneering work on etching-during-growth using a F-based plasma chemistry [9]. They found that the presence of ion bombardment, achieved by growing films on the cathode of an RF glow discharge reactor, led to a dramatic change in crystallinity of the films deposited from a SiF_4+H_2 mixture.

REFERENCES

1. F. Okumura et al, Proc. Materials research Society, <u>377</u>,877(1995)

2. J. Symons et al, Proc. of Materials Res. Society, <u>95</u>,621(1987)

3. J. Meire et al, Appl. Phys. Lett. <u>65</u>,860(1994)

4. U. Kroll et al, Proceedings of Materials Res. Soc., <u>377</u>,39(1995)

5. V. L. Dalal et al, Proc. Materials Res. Soc., <u>377</u>, 137(1995)

6. S. G. Burns et al, J. Electrochem. Soc.,2nd. Symposium, Proc. <u>94-35</u>, 370(1994)

7. D. P. Grimmer et al, Int. J. Solar Energy, <u>18</u>, 205(1996)

8. V. L. Dalal et al, Appl. Phys. Lett., <u>64</u>,1962(1994)

9. V. L. Dalal et al, Proc. of American Inst. of Physics, <u>Vol. 73</u>, 15(1981)

10. S. Lee, S. Kumar and C. Wronski, J. Non-Cryst. Solids, <u>114</u>, 316(1989)

REFERENCES CITED

1. Liboff, R., *Introductory Quantum Mechanics*, 2nd Ed. (Addison Wesley, New York, 1992).

2. Singh, J., *Optoelectronics, An Introduction to Materials and Devices*, (McGraw Hill, St. Louis, 1996).

3. Kanicki, J., *Amorphous and Microcrystalline Devices - Materials and Device Physics*, (Artech House, Norwood, MA, 1991).

4. Moller, H., *Semiconductors for Solar Cells*, (Artech House, Boston, 1993).

5. Dalal, V., "Comprehensive research on stability of amorphous silicon and alloy materials and devices," *Final Subcontract Report NREL/XAN 4 13318 08*, (1996).

6. Geller, R., *Electron Cyclotron Resonance Ion Sources and ECR Plasmas*, (Institute of Physics Publishing, London, U.K., 1996).

7. Asmussen, J., "Electron cyclotron resonance microwave discharges for etching and thin-film deposition," *J. Vac. Sci. Technol. A* **7**, 3 (1989).

8. Mort, J., and Jansen, F., *Plasma Deposited Thin Films*, (CRC Press, Florida, 1986).

9. Konuma, M., *Film Deposition by Plasma Techniques*, (Springer-Verlag, Berlin, 1992).

10. National Materials Advisory Board, *Beam Technologies for Integrated Processing*, (National Academy Press, Washington, D.C., 1992).

11. Lieberman, M., and Lichtenberg, A., *Principles of Plasma Discharges and Materials Processing*, (Wiley Interscience, New York, 1994).

12. Kaushal, S., "Growth of highquality a-(Si,Ge):H films using low pressure, remote ECR plasma technique," Master's Thesis, Iowa State University, (1995).

13. Deboer, S. and Dalal, V., "Low temperature epitaxial silicon growth using high vacuum electron-cyclotron-resonance plasma deposition," *Appl. Phys. Lett.* **66**, 19 (1995).

14. Parsons, G., "Microstructural evolution and substrate selectivity in PECVD μC-Si," *MRS Symp. Proc.* **283**, 495 (1993).

15. Lee, S., Kumar, S., and Wronski, C., "A critical investigation of a-Si:H photo conductivity generated by sub-gap absorption of light," *J. Non-Cryst. Solids*, **114**, 316 (1989).

16. Meier, J., Fluckiger, R., Keppner, H., and Shah, A., "Complete micro-crystalline *p-i-n* solar cell—Crystalline or amorphous cell behavior," *Appl. Phys. Lett.* **65**, 860 (1994).

17. Kiagawa, M., Setsune, K., Manabe, Y., and Hirao, T., "Preparation of doped hydrogenated amorphous silicon films by microwave electron-cyclotron-resonance plasma discharge deposition," *J. Appl. Phys.*, **61**, 5 (1987).

18. Hecht, *Optics*, 2nd Ed.(Addison and Wesley Publishing, New York, 1990).

19. Herman, I. P., *Optical Diagnostics for Thin Film Processing*, (Academic Press, New York, 1996).

20. Burke, H. and Herman, I. P., "Laser photochemical deposition of germanium-silicon alloy thin films," *Appl. Phys. Lett.*, **55**, 253 (1989).

21. Dr. George Chumanov, (Personal discussions and Raman spectroscopy measurements,) Dept. of Chemistry, Iowa State University.

22. Fischer, D., Dubail, S., Selvan, J. A., Vaucher, N., Platz, R., Hof, Ch., Kroll, U., Meier, J., Torres, P., Keppner, H., Wyrsch, N., Goetz, M., Shah, A., and Ufert, K.D., "The micromorph solar cell: extending A-Si:H technology towards thin film crystalline silicon," *25th IEEE PV Spec. Conf.,* Washington, (1996).

23. Ganguly, G., Ikeda, T., Nishimiyra, T., Saitoh, K., Kondo, M., and Matsuda, A., "Hydrogenated microcrystalline silicon germanium: A bottom cell material for amorphous silicon-based tandem solar cells," *Appl. Phys. Lett.* **69**, 27 (1996).

24. Mittal, K., and Ghosh, M., *Polyimides Fundamentals and Applications*, (Marcel Dekker Inc., New York, 1996).

62

ACKNOWLEDGEMENTS

I would like to take this opportunity to thank the various people who have helped me complete this investigation.

First and foremost, my sincere gratitude goes out to my major professor Dr. Vikram Dalal for his invaluable guidance and support throughout this research project. I would also like to thank Dr. Gary Tuttle and Dr. Howard Shanks for serving on my committee. Dr. George Chumanov deserves kudos for his help in performing the necessary Raman spectroscopy measurements. Thanks also go out to members of Iowa Thin Films for providing me with various types of polyimide substrates.

I would like to thank the Iowa State University Department of Electrical Engineering, National Renewable Energy Laboratory, and Electric Power Research Center for providing financial support during the past 2 years of my work at the Microelectronics Research Center. Without their help I would not have been able to pursue an advanced degree.

I would also to thank Dr. Sanjeev Kaushal, Dr. Ralph Knox, Tim Maxson, Jason Herrold, Sohail Haroon, Phillip Espinasse, Kequin Han, Sandya Gupta, Shi Di Cheng, Jon Kavanaugh, Bryan Oliver, Adam Sanford, Al Landin, Dave Schmidt, and Jane Woline for their friendship, guidance, support and interesting discussions.

Special thanks goes out to my former professors at Gustavus Adolphus College for the education they provided in preparing me for graduate studies. A job well done!

Finally, I would like to thank my wife, Deb, and our families for their patience, support and love during this educational and time consuming experience.